Advances in Material Research and Technology

Shadia Ikhmayies *Editor*

Advanced Semiconductors

Springer

Advances in Material Research and Technology

Series Editor

Shadia Jamil Ikhmayies, Department of Physics, School of Science, University of Jordan, Amman, Jordan

This Series covers the advances and developments in a wide range of materials such as energy materials, optoelectronic materials, minerals, composites, alloys and compounds, polymers, green materials, semiconductors, polymers, glasses, nanomaterials, magnetic materials, superconducting materials, high temperature materials, environmental materials, Piezoelectric Materials, ceramics, and fibers.

Shadia Ikhmayies
Editor

Advanced Semiconductors

Springer

Editor
Shadia Ikhmayies
Department of Physics, School of Science
University of Jordan
Amman, Jordan

ISSN 2662-4761 ISSN 2662-477X (electronic)
Advances in Material Research and Technology
ISBN 978-3-031-88282-1 ISBN 978-3-031-88283-8 (eBook)
https://doi.org/10.1007/978-3-031-88283-8

This Springer imprint is published by the registered company Springer Nature Switzerland AG
The registered company address is: Gewerbestrasse 11, 6330 Cham, Switzerland

Preface

Semiconductors represent a category of the advanced materials used in high-tech applications and are the building blocks of electronic devices. Without semiconductors, digital devices could not work or might not exist at all, because semiconductor chips are what power the digital age. Semiconductors form the basis of modern computing devices such as smartphones and laptops, and form the backbone of the Internet, enabling global connectivity. Overall, semiconductors have been a driver of advances in communications, computing, healthcare, clean energy, transportation, military systems, and countless other applications. This book covers recent developments in the research and technology of semiconductor materials and their applications. It brings together materials design, modeling and numerical computations, with experimental synthesis, processing, characterization and industrial uses in a comprehensive resource. The comprehensive nature of the book makes it an indispensable source of information for researchers, graduate students, scientists, and post-graduate students in the field of physics, material science, photovoltaics, and electronic engineering. A wide range of topics are covered and discussed in this book as briefly described in the following paragraphs.

Chapter one, "Overview of Modern Inorganic, Organic, and Hybrid Semiconductors" by Sumona Sinha et al. provides an extensive survey of the recent important research work on the electronic and optical properties of the current advanced semiconductors. Several inorganic compounds and alloys, low-weight organic semiconductors, lower-toxic lead-free halide hybrid perovskites and beyond graphene 2D semiconducting materials are discussed through complementary experimental and theoretical approaches. The discussions are presented on the basis of a careful survey of recent vital advances in various electronic and optoelectronic devices (e.g. light emitting diodes (LEDs), photocells, photodetectors, field effect transistors (FETs), and sensors). This chapter may help to stimulate further new avenues of basic research as well as technological advances. Chapter two, "Morphology-Dependent Properties in Inorganic Semiconductors: An Experimental and Theoretical Approach" by Amanda Fernandes Gouveia et al. presents an experimental and theoretical approach to address the morphology-dependent properties of inorganic semiconductors. The Ag-based metal oxide semiconductors have been

investigated by combining experimental studies and simulations based on first-principles calculations. It is expected that the calculations can provide valuable hints for improving the performance of metal oxide semiconductors, and the morphology may lead to significant progress in advancing new applications on many fronts.

Chapter three, "Semiconductor Physics: A Density Functional Journey" by Sujoy Datta and Debnarayan Jana reviews the study of semiconductors using density functional theory. The chapter starts with the fundamentals from Local Density Approximations (LDA) to the most recent developments of semi-local corrections [Generalized Gradient Approximation (GGA, Meta-GGAs], including hybrid functionals and orbital dependent methodologies. The authors point to the success of semi-local approximations in predicting structural properties of materials. The comparison of energy-dependent Fermi properties can guide theoretical studies on recent eco-friendly research on semiconductors, such as artificial photocatalysis, energy-saving optoelectronic devices, etc. The appropriate choice of the DFT method is likely to be eligible to complement the experimental results and may also open a path for advanced semiconductor material discoveries. Chapter four, "Tuning the Electron Transport Properties of Nanotube Semiconductors" authored by Hui Li et al., reports a series of methods for converting metallic nanotubes into semiconductors. These methods include the atomic depression of boron nanotubes (BNT), and rotation of the inner boron phosphide tube (BP) in boron arsenide (BAs)/BP heterojunctions of nanotubes, and tuning the electronic properties of nanotubes of black phosphorus by doping, and building heterojunctions of ferromagnetic half metallic Fe_2Si nanotubes and carbon nanotubes (CNTs). The most exciting influence of these treatments on nanotubes is the appearance of strange properties such as negative differential resistance (NDR), and ferromagnetic properties, which have potential applications in logic circuits.

Chapter five, "2D Transition Metal Ditellurides: Synthesis, Properties, and Applications" by Ishant Chauhan et al., provides developments of structure, synthesis approaches, and potential applications of $MoTe_2$ and WTe_2 as transition metal ditellurides. A wide range of functional applications in various fields are discussed, including flexible electronics, laser absorption, photodetection, and sensing as well as storage of hydrogen energy. After reading this chapter reader will have more accurate information to further explore the different properties of these materials. Chapter six "Application of Oxide and Chalcogenide Semiconductor Films in Photoelectrochemical Reduction Reactions", by Moisés A. de Araújo et al., presents the recent developments in chalcogenide (i.e. sulfides and selenides), and oxide-based semiconductor materials used in photoelectrochemical (PEC) cells' applications. Furthermore, the technological significance of such materials, especially with regard to their applications in PEC cells, is discussed in order to stimulate the improvement in the design of new advanced semiconductor materials. Chapter seven "The Formation and Utilization of Defects and Tracks During the Ion Implantation of Diamond and c-BN Thin Films" by Ariful Haque covered the present understanding of the inherent physical processes during the modification of the structural and electronic properties of the two ultrahard materials; cubic boron nitride (c-BN) and diamond using ion implantation process. The chapter covered the generation of defects, formation of the

tracks, and inhomogeneity of the atom density through these two super hard crystals during the ion implantation process. Special attention is given to avoid the energetic ion induced graphitization during the high energy ion implantation process of these sp^3 bonded super hard and versatile materials.

Finally, chapter eight, "Thermomechanical Response on a Reflection Photothermal Diffusion Waves of a Rotating Magneto-Semiconductor Medium" by Kh. Lotfy and A. El-Bary investigated a model for the reflection of a coupled and a rotational waves from a rotating magnetized elastic semiconducting medium, where the coupled wave consists of thermal wave, elastic wave, plasma wave, and diffusion wave. The governing equations were obtained using the photothermal transfer process during the mass diffusion in the rotating medium. The authors used the harmonic wave approach to find the reflection coefficients, and applied mechanical and thermal stresses to the free surface of the elastic semiconductor material. The relationships between the reflection coefficients and angle of incidence are computed numerically and represented graphically to show the influence of many parameters such as magnetic field, rotation frequency, and others during the diffusion p rocesses.

Amman, Jordan Shadia Ikhmayies

Contents

Overview of Modern Inorganic, Organic, and Hybrid Semiconductors

Sumona Sinha, Susmita Jana, and Debnarayan Jana

Abstract The semiconducting material is always at a pivotal point in the development of electronics as well as optoelectronics. In the last two decades of the present century, especially in the past 10 years, interdisciplinary research focused on the fundamental studies of semiconductors and the design of corresponding devices. In this time, several inorganic compounds and alloys, low-weight organic semiconductors (OScs), lower-toxic, lead-free halide hybrid perovskites, and beyond graphene 2D semiconducting materials are exhibiting their potential. This chapter deals with an extensive study of the recent important research works on the electronic and the optical properties of the modern semiconductors by complementary experimental and theoretical methods. Both properties are indispensable for understanding as well as optimizing functionality and performance of semiconducting devices. To address these issues, a general discussion on the basis of a comprehensive survey on recent significant development of several electronic and optoelectronic devices has been presented. This chapter may help to trigger further new avenues for fundamental research as well as technological progress.

Keywords Inorganic semiconductors · Organic semiconductors · Hybrid semiconductors · Two dimensional (2D) semiconductors · Electronic properties · Optical properties · Device applications

1 Introduction

Semiconductors are at the heart of the development of modern electronics and digital technology. The study of semiconductor physics and devices have emerged from early nineteenth century and experienced steady progress since the middle of the

S. Sinha · S. Jana · D. Jana (✉)
Department of Physics, University of Calcutta, Kolkata, India
e-mail: djphy@caluniv.ac.in

S. Sinha
Department of Basic Science and Humanities, Institute of Engineering and Management, Newtown, University of Engineering and Management, Kolkata, India

S. Ikhmayies (ed.), *Advanced Semiconductors*, Advances in Material Research and Technology, https://doi.org/10.1007/978-3-031-88283-8_1

twentieth century. With the invention of the transistors by Shockley, Bardeen, and Brattain in 1947, inorganic semiconductors such as silicon or Germanium started to take over the role of the omnipresence material in electronics from the previously prevailing metals. The tuning of electrical properties of semiconducting materials by external parameters—such as light, applied electric-field, magnetic-field, temperature, or mechanical pressure—make the semiconductor an attractive candidate for electronic devices, many of which have become indispensable parts of human daily lives such as computers, storage devices, displays, and optical communications. It made possible to realize integrated circuits (IC) on a single piece of silicon. In the form of a very large-scale integrated circuits (VLSI), it provided a gigantic boost in speed while at the same time scaled-down the size of these electronic devices. Along the reduction of the size of the devices, an alternative material to silicon which is stable, environmentally friendly, strong but flexible, is continuously attracting significant research interest for future generation devices [1, 2]. Now at the beginning of the twenty-first century, we are facing a new electronics revolution that has become feasible due to the progress as well as an understanding of notably three new classes of materials, namely organic semiconductors, organic-inorganic hybrid perovskites and two dimensional (2D) semiconductors [3, 4]. The advancement in this field is driven by the prospect of these materials with new applications, such as large-area flexible light sources, displays, and low-cost, high-speed printed integrated circuits or plastic solar cells. The history of the electronics industry over the previous few decades has been mostly an elaboration of Moore's Law (prediction made by American engineer Gordon Moore in 1965), that is, the number of transistors which can be fabricated in a given area of a semiconductor chip doubles around every 24 months. The success of the semiconductor industry depends on the production of ever-more-complex circuits with decreasing cost per circuit element.

Hence, a thorough understanding of their operation needs a detailed study of the physical (such as electronic, optical, transport, etc.), and chemical properties of the semiconductor components. In several respects, the transport properties of the semiconductors require sophisticated knowledge based on the information about the electronic structure of the system. Moreover, electronic properties provide a background for the optical properties of the semiconductors whereas the progress of optoelectronic devices is one of the main focus of researchers nowadays. To make further development of such devices the understanding as well as the control of the electronic and optical properties of modern prospective semiconductors are very crucial.

2 Inorganic Compound and Alloy Semiconductors

2.1 Materials

Besides the elemental semiconductors such as, C, Si, Ge, Sn, etc. alloy semiconductors can be made by compounding together certain groups of elements. These compound systems can be divided into other categories depending on the number of elements present in the systems. These are binaries (with two atoms of groups III–V's; II–IV's; IV–VI's; I–VII's), ternaries (with three atoms), quaternaries (with four elemental atoms) and so on. Compound semiconductors exhibit a wide range of band gaps and are of great interest in optical communications. Various binaries (such as GaAs, ZnS, PbSe, InP, SiC, etc.), ternaries (AlGaAs, InGaAs), and quaternaries (InGaAlAs, InGaAsP and AlGaAsSb) have been synthesized to serve the purpose. These inorganic compounds have some advantages over elemental semiconductors. Most of them have direct or, indirect band gaps and cover a wide range of band gaps at discrete k points. They follow definite trends and can be grown in bulk form and cut into wafers for interesting characterizations. Alloy semiconductors can be constructed by adding a small quantity of a third element to the alloy mixture, such as, gallium aluminum arsenide ($Al_xGa_{1-x}As$) [5]. The subscript x or, y refer to the alloy content of the material, or the proportion of the material that is replaced by the alloying material. Some examples of alloy semiconductors are gallium indium arsenic phosphide ($Ga_xIn_{1-x}As_yP_{1-y}$) or gallium indium nitrogen arsenide (GaInNAs) and even quinternary materials such as gallium indium nitrogen arsenic antimonide (GaInNAsSb) [6]. This is an efficient way to modulate the energy gap and lattice properties of the crystals to suit various applications [7].

2.2 Electronic Properties

The opto-electronic properties of materials are governed by the characteristics of the distribution of electron energy states in each semiconductor. Doping of an intrinsic semiconductor has significant effects on changing the energy states to serve a definite purpose. All the binary semiconductors of group II–VI [5], III–V [6] are wide band gap direct or, indirect semiconductors with band gap in the range of 1–4 eV. There are a total of 8 outer electrons per unit cell which contribute to the chemical bonds. The other electrons are "frozen" in closed shell configurations and their wave functions are tightly bound to their nuclei. They do not contribute to the electronic properties. As an example of binary semiconductor, in GaAs the 8 outermost electrons (3 from Ga and 5 from As) hybridize to form tetrahedral bonds between one kind of atom (say Ga) and its four nearest neighbors (As) [8]. The orbitals of every atom hybridize with any one orbital of the neighboring atom, producing two bonding and antibonding energy levels. The band structure is shown in Fig. 1 with contrast to that of elemental Si structure.

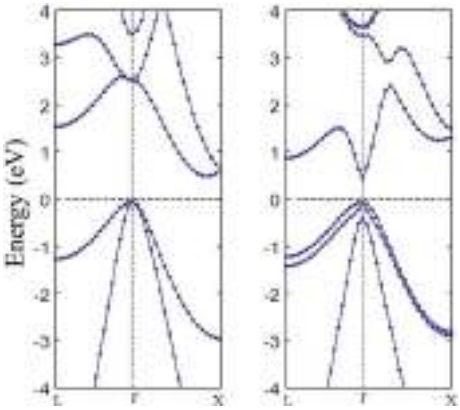

Fig. 1 Energy band spectra of **a** Si and **b** GaAs. Redrawn after Sze [8]

In the case of ternary and quaternaries, their electronic band spectra depend on the percentage of elementary atoms present in the alloy. The bandgap of III–V ternaries usually follow a quadratic dependence on the alloy composition x. For $Ga_xIn_{1-x}As$, $InAs_xSb_{1-x}$ and $Ga_xIn_{1-x}Sb$ ternaries there exists a direct-indirect bandgap crossover for $x = 0.7$ (as shown in Fig. 2). Nitrogen incorporation into (In,Ga)(P,As) results in a sufficiently large band gap which increases with increasing nitrogen concentration [6]. Among recent research, the quaternaries of $Cu_2ZnSiVI_4$ (VI = S, Se, and Te) have drawn widespread attention due to their inexpensive and environmentally friendly elements and wide range of energy gaps [9]. These band gaps generally decrease with increasing anion atomic number. The band gaps are 3.02, 1.97, and 1.37 eV for Cu_2ZnSiS_4, $Cu_2ZnSiSe_4$ and $Cu_2ZnSiTe_4$ respectively. This is due to the fact that the valence band maximum is composed of group VI p and Cu 3d states. These materials are considered to have potential applications in photovoltaic, thermoelectric and optoelectronic devices. In II–VI ternary alloys, replacing existing atom with high atomic number results in the decrease of the energy gaps due to the increase of charge carriers.

Apart from elemental alloying, formation of heterojunctions with known semiconducting materials also gives rise to interesting electronic properties. If a heterojunction is made with two materials, such as GaAs and AlAs (as $Al_xGa_{1-x}As$ exists for all x such that $0 \leq x \leq 1$), the chemical transition between these materials does not occur abruptly. Such heterojunctions have desirable properties for optoelectronic applications. This kind of heterostructures are able to improve the performance of semiconductor devices.

2.3 Optical Properties

In case of homopolar semiconductors such as Si and Ge, the fundamental vibration has no dipole moment and is infrared inactive. But, in heteropolar semiconductors,

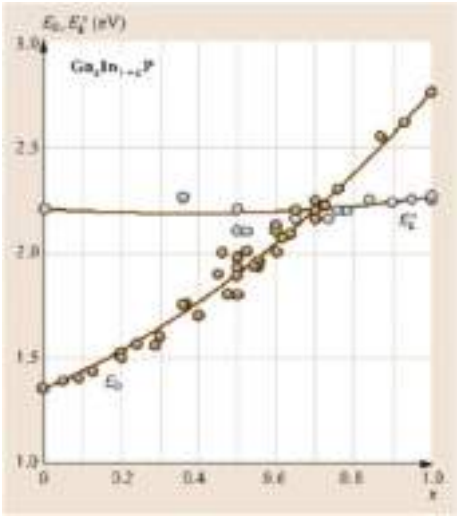

Fig. 2 Variation of direct and indirect energy gaps in the $Ga_xIn_{1-x}As$ ternary with the concentration of alloys. There is a crossover for $x = 0.7$. Reprinted from Adachi [6], with permission from Springer International Publishing AG. Copyright (2017)

such as GaAs and InP, the first-order dipole moment gives rise to a very strong absorption band associated with the long wavelength optical modes. Below this band, the real part of the dielectric function asymptotically approaches the static or low-frequency dielectric function. The band gap energies of II–VI and III–V groups of semiconductors are in the range of 0–5 eV [10–12]. The refractive index (n) of a semiconductor with definite energy gap (E_g) is given by various popular relations such as Tripathy relation (Eq. 1), Moss relation (Eq. 2), Ravindra relation (Eq. 3), etc. [13].

$$n = n_0\left[1 + \alpha e^{\beta E_g}\right] \tag{1}$$

$$n^4 E_g = 95\,\text{eV} \tag{2}$$

$$n = 4.084 - 0.62E_g \tag{3}$$

In Eq. (1), n_0, α and β are fit parameters while experimental values of n are fitted to exponential function. These relationships work efficiently within the energy gap range $0 < E_g < 5$ eV. The complex dielectric function $\epsilon(\omega)$ values are also calculated using $n = \sqrt{\epsilon(\omega)}$, where ω is the angular frequency. It can be observed from Fig. 3 that, the dielectric function decreases with the increase in energy gap. The theoretical trends of the calculated dielectric functions fairly match with the experimental trend. In general, reflectivity of these materials decreases with the energy gap and fairly follows a linear trend. For the ternary semiconducting alloys such as CdS_xSe_{1-x}, $CdSe_{1-x}Te_x$, $Zn_{1-x}Hg_xTe$, $Cd_xHg_{1-x}Te$, the energy gaps vary with alloy concentration (x), resulting in varying amounts of absorbance at different

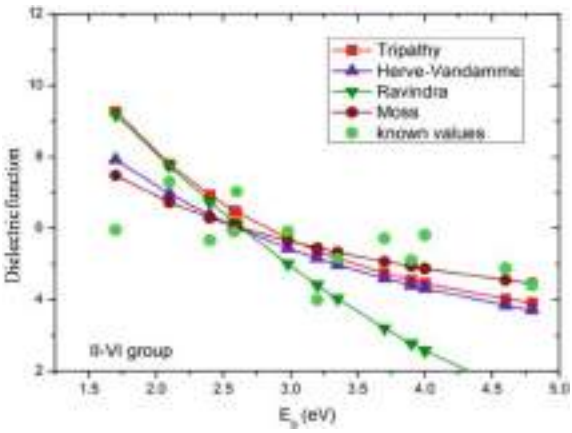

Fig. 3 Dielectric function of group II–VI semiconductors at low frequency as a function of the band gap energy as given by different equations and experimental known values. Reprinted from Tripathy and Pattanaik [13], with permission from Elsevier. Copyright (2016)

wavelengths [14, 15]. The other optical properties such as the refractive index, and optical polarizability increase by adding small amounts of electro-negative ions.

Apart from these well-known binary and ternary semiconductors, new compound materials have gained much attention due to their enhanced optoelectronic properties. The optical properties of $SrPbO_3$ and their Fe doped structures have conveyed excellent absorption at visible light spectra [16]. The calculation of dielectric function and conductivity exhibits a conducting behavior in the low energy range of the light spectrum, and the Fe doping by 6% of $SrPbO_3$ leads to superconducting behavior.

The dependence of the refractive index, high-frequency dielectric function, and electron charge distribution of AlP_xSb_{1-x} [17] shows non-linear behavior with composition. Also, the band gap of the semiconductor was found to depend on the concentration of P. The behavior of the high-frequency dielectric function indicated that this material behaves as a good insulator when more P atoms are incorporated. The optical constants for zinc blende-derived structures of $Cu_2ZnSiVI_4$ (where VI $\equiv$ S, Se, Te) [9] show similar trends over a broad range of energy. Moving on to the absorption coefficient, we can notice that the same applies to all the quaternary compounds, it is quite large ($\sim 10^4$ cm^{-1}), and at a given energy, Te compounds have larger absorption coefficients than S and Se compounds. Comparing with the calculated spectra of other materials, it is found that the value of the absorption coefficient α increases in this sequence, $\alpha(Cu_2ZnSiX_4) > \alpha(Cu_2ZnGeX_4) > \alpha(Cu_2ZnSnX_4)$ which indicates that the compounds with heavier group-IV elements should have higher light transformation efficiency [9].

2.4 Applications: Field-Effect Transistors (FETs), Solar Cells, and Light-Emitting Diodes (LEDs)

Regarding Field-effect transistors (FETs) there are many recent studies on various applications. Among the recent studies on general inorganic semiconductors that have been made by the eye-grabbing observations is the study of Simoni et al., on metallic supercurrent FET [18]. Their findings on Ti-based FETs expose the substantial bipolar impact of a static electric field on a superconducting film. For memory device purposes, an interesting study is performed on ferroelectric FET (FeFET) by Tsai et al. [19], where a flexible FeFET composed of oxide heteroepitaxy on muscovite was achieved by combining an Al-doped ZnO film as the semiconductor channel layer and a $Pb(Zr_{0.7}Ti_{0.3})O_3$ film as the ferroelectric gate dielectric. The smallest bending radius that was recorded was 5 mm with a cyclability of 300 times, and retention of 100 h. Oh et al. [20] reported the bottom-up integration of a 1D–2D hybrid semiconductor nanostructure into a vertical FET for use in flexible inorganic electronics. This FET exhibits a small subthreshold swing of 110 mV dec^{-1}, a high current I_{max}/I_{min} ratio of 10^6, and a transconductance of 170 nS μm^{-1}. Furthermore, SnO_2/ZnO hetero nanostructures are capable to detect H_2S gas as low as 10 ppb concentration [21].

In the case of inorganic and alloyed semiconductors, first-principles calculations provide valuable information about materials used in solar-cell technology. The results have revealed the phase diagrams, band gaps, and bowing parameters of $CuIn_xGa_{1-x}Se_2$ and $CuAl_xGa_{1-x}Se_2$ [22]. Other studies have focused on earth-abundant materials of the CZTS (copper-zinc-tin-sulfide) family, such as Cu_2ZnSnS_4 and $Cu_2ZnSnSe_4$ [23]. CIGS is mostly used as a light absorber for thin-film solar cells. Ga and In used in CIGS solar cells are rare and expensive materials. Instead of that thin films made from CZTS have lower manufacturing cost, The Zn–IV–V_2 compounds (such as, $ZnGeN_2$ and $ZnSnN_2$) are another class of earth-abundant solar-cell materials [24] with band gaps equal to 3.42 eV and 2.02 eV respectively. Moreover, the predicted band gap of $ZnSnP_2$ is reduced by 0.95 eV between the ordered chalcopyrite and the cation-disordered sphalerite structure. This reveals the fact that tuning of the order parameter in phase transition can be exploited to adjust the band gap for solar-cell applications.

3 Organic Semiconductors

3.1 Materials

Organic semiconductors have been studied for about 100 years ago. The discovery of photoconduction in anthracene in 1906 can be referred to as the beginning of organic semiconductor (OSc) research [3, 25]. The semiconducting properties of organic semiconductors originates from the presence of conjugated π bonds in their

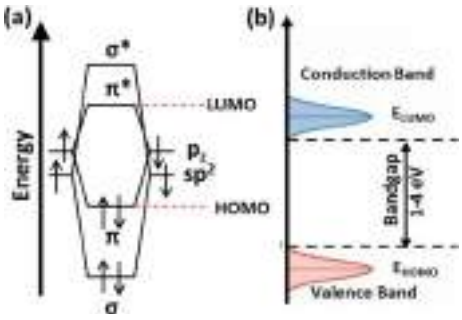

Fig. 4 Schematic representation of **a** the energy level diagram illustrating the bonding and, antibonding levels and formation of HOMO, LUMO, and **b** their corresponding band gap. Part **b** reprinted from Bronstein et al. [26], with permission from Springer Nature. Copyright (2020)

molecular structure. The conjugated double bonds formed by C atoms are of sp^2 hybridized character which give rise to both σ and π bonds. The energy levels are then, split into occupied bonding orbitals with lower energy, and unoccupied anti-bonding orbitals of higher energy. This is illustrated schematically in Fig. 4. The charge transfer or optical excitation mechanisms are therefore mostly contributed by the electronic states (π orbitals) closest to the Fermi level.

The materials with larger number of conjugated C atoms, π-electrons are highly delocalized and the number of bonding and anti-bonding π-orbitals increases. The band gap of organic semiconductors corresponds to the HOMO–LUMO gap in their molecular orbitals, as shown in Fig. 4. Organic semiconductors are also available in p-type, n-type, and ambipolar. In the case of organic semiconductors, the p-type is that where holes (electron-deficient species) act as charge carriers and the n-type semiconductor is that where electrons (electron-abundant species) are the charge carriers, whereas in the ambipolar case, both p-type, as well as n-type segments, are incorporated in a single molecule. As the charge carriers are localized, the doping level and the doping mechanism for organic semiconductors are different from their inorganic counterpart [27–29].

Organic semiconductors are typically divided into three main categories based on their complexity: small molecules, polymers, and biological materials. Only small molecules and polymers have been practically used in functional organic electronic devices. Small molecule semiconductors, oligomers, consist of molecules with well-defined molecular weights, while polymers are characterized by long, flexible chains of repeating units with variable chain lengths. Although oligomers and their corresponding polymers differ in their molecular weights, their electronic and optical properties are often quite similar. However, the key differences arise in the methods of film formation and device fabrication. Polymers have the advantage of solubility, allowing for cost-effective production techniques such as spin-coating and ink-jet printing. In contrast, small molecules, which are generally insoluble, require more complex deposition methods, resulting in higher costs. Nevertheless, small molecules offer the advantage of forming films with high purity and crystalline structure, essential for achieving superior charge carrier mobility. So we give our concern on the electronic as well as optical properties of small molecules and their device applications in the present chapter. Figure 5 displays the molecular structures of some prototype

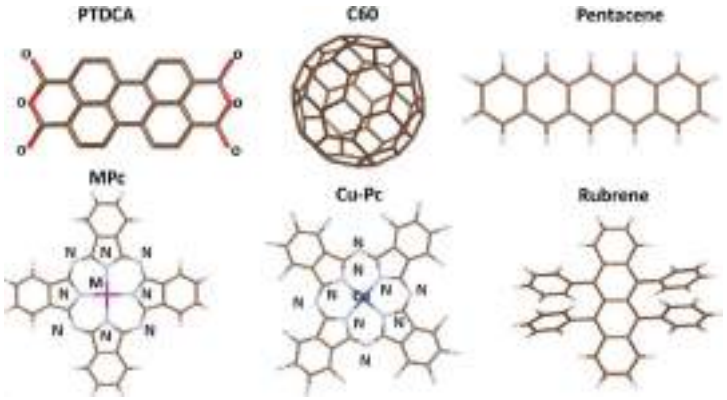

Fig. 5 Molecular structure of some prototype organic semiconductors: perylene-3,4,9,10-tetracarboxylic dianhydride (PTCDA) ($C_{24}H_8O_6$), fullerene (C_{60}), pentacene($C_{22}H_{14}$), metal phthalocyanine (MPc), F_{16}CuPc (copper hexadecafluorophthalocyanine), rubrene ($C_{42}H_{28}$)

low-weight organic semiconductors those are currently showing high carrier mobility as well as promising characters in their optical behavior [30, 31].

3.2 Electronic Properties

The property which distinguishes semiconductors from other materials, as well as between various semiconductors, concerns the behavior of their electrons, in particular the existence of gaps in their valence and conduction electronic spectra.

During the last few years, there has been reported a lot of experimental and theoretical studies on organic/inorganic interfaces in the literature. The majority of experimental studies were performed using photoemission spectroscopy. Moreover, it is noteworthy to mention here that thin films are suitable in the field of flexible and lightweight device applications. In addition, the high-cost, inflexibility, and difficulty of fabricating large-area single-crystal limit its application in practical devices. Low pressures around 10^{-9} mbar and slow deposition rates around several Å/min, as well as the variation of the substrate temperature during growth, enable control over thickness, composition, and structural ordering [3, 29]. Hence, we focus mostly on the ultra-high vacuum (UHV) grown thin film samples.

The junction between the organic semiconductors and other materials, i.e., the interface occurs within the first monolayer of the organic semiconducting side is one of the attractive issues to the scientific community. The major interesting change in basic properties (such as electronic, structural, chemical, and optical) of the considered system is found to take place within a monolayer of organic semiconducting film. Then the properties are gradually saturating with increasing number of monolayers to those of organic bulk counterpart. In addition, the charge carrier transport of organic

thin film transistors (OTFTs) occurs at first organic monolayer, in contact with gate dielectrics whereas charge injection into an organic active layer occurs at organic/metal interfaces. Hence, the study of the organic monolayer is a more exciting one in fundamental as well as technical aspects. In fact, in the case of organic semiconductor thin films, the researches have paid attention to investigate the basic properties of the considered system by stepwise depositing organic semiconductor on a substrate [3, 28].

In this chapter, as an example, we first discuss studies of the interfaces between rubrene (5,6,11,12-tetraphenyltetracene) and Au, Ag, H passivated and SiO_2 coated Si (100) substrates using X-ray spectroscopy (XPS) and UV photoemission spectroscopy (UPS). The energy level shift was found as more prominent at first rubrene monolayer then it was gradual. The results of this investigation suggested that the thickness-dependent energy level alignment of the physisorbed rubrene films onto the above-mentioned substrates can be explained by a dielectric model in terms of photoemission final state relaxation energy [32, 33]. Moreover, the vacuum level (VL) of Au and Ag also more significantly observed to shift with rubrene film thickness in the monolayer range. This VL shift indicated that the interface dipole was confined in the rubrene monolayer which originated due to the push-back effect. Next, we consider discussing the interfacial energetics in presence of chemical interaction. It has been shown for the interfaces in between of CuPc thin films and coinage metal (Au, Pt, Ag, and Cu) substrates that the pyrrole sites of CuPc molecules are influenced due to partial charge transfer from Cu and Ag substrates. Whereas an insignificant impact on these sites was obtained for Pt and Au ones. In addition, for this charge transfer, a hybridized state near Fermi level, F-LUMO (as shown in Fig. 6, was found to appear at sub-monolayer coverage). The partial electron transfer is more significant on Cu surfaces than Ag. No notable F-LUMO was exhibited for other cases. The partial charge transfer did not play the governing role over push back in the VL shift; origin of the monolayer confined interface dipole [34]. In the case of the experimental investigation about PTCDI/Ag interfaces, Emanuelsson et al. have noted [35] that the adsorbate/substrate interaction vigorously alters the electronic configuration of the PTCDI molecules at their first monolayer coverage compared to that of higher ones. This interfacial interaction at their first monolayer coverage basically results in extra states above the regular PTCDI HOMO level as well as the splitting of HOMO and LUMO levels.

Next, we consider CuPc/ferroelectric-polymer interfaces. As polymer poly(vinylidene fluoride—trifluoroethylene) P(VDF-TrFE) and poly(vinylidene fluoride—trifluoroethylene—chlorofluoroethylene) P(VDF-TrFE-CFE) are chosen on the basis of their realistic applications. It has been experimentally observed that the work function and HOMO level shift with successive CuPc deposition because of the emptying of tailing states from CuPc HOMO. This occurs due to the electron transfer from CuPc to ferroelectric polymer and leads to the formation of the interface dipole [36]. All these phenomena mostly occurred in CuPc monolayer. In the case of $F_{16}CuPc/TiO_2$ interface, the presence of strong coupling between the molecules and the TiO_2 surface is observed. Adsorbed molecules experience substrate mediated charge transfer. Electrons being pulled away from nitrogen

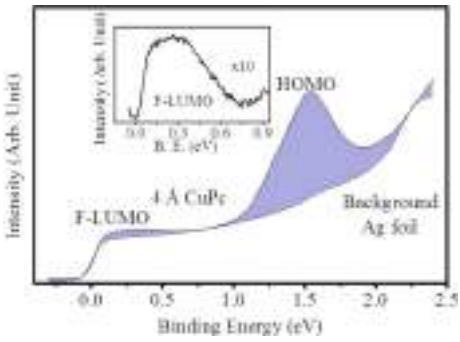

Fig. 6 UPS spectra of the clean Ag substrate and the near Fermi region of 4 Å thick CuPc films; the inset displays the F-LUMO magnified 10 times with metallic background subtracted [34]

atoms toward carbon ring. Near Edge X-ray Absorption Fine Structure (NEXAFS) spectroscopy in combination with resonant photoemission spectroscopy (RPES) provides a direct measure of charge transfer dynamics. Using these combined synchrotron-based spectroscopy techniques (shown in Fig. 7), The evolution of XPS-UPS spectra with F_{16}CuPc film thickness from sub-monolayer to multilayer exhibits a strong coupling between the adsorbate molecules and the TiO_2 surface. Ultrafast charge transfer from molecules of monolayer thick F_{16}CuPc film to the TiO_2 substrate is found to take place on the time scale of 10 fs due to their strong electronic coupling [37].

Next, we concentrate on organic semiconductor/2D semiconductor interfaces for discussion. Feng et al. [38] reported their observation of phthalocyanine/graphene interfaces from density functional theory-van der Waals (DFT-vdW) calculation that the adsorption of Pc and MPcs (M = Cu, Fe, Zn, and Sn) is unable to open the gap of graphene. Typical total density of states (DOS) of graphene, SnPc/graphene, CuPc/graphene, and FePc/graphene are exhibited in Fig. 8. On the other hand, the adsorption of MPc molecules is found as stronger on the MoS_2 monolayer surface than graphene and significantly modify the MoS_2 electronic structure from the density functional theory (DFT) calculation of Haldar et al. [39]. In 2020, Greulich and his coworkers [40] carried out an experimental investigations on interface properties between MoS_2 and differently fluorinated iron phthalocyanines ($FePcF_x, x = 0, 4, 16$) using a combination of various photoelectron spectroscopies and X-ray absorption spectroscopy (XAS).

They have revealed that a crucial parameter for the interfacial charge transfer is the ionization potential of $FePcF_x$. The charge transfer is responsible for the formation of a large interface dipole, gap-states at the $FePcF_x/MoS_2$ interface and a band bending in the MoS_2 substrate. Nowadays, an eye-grabbing research topic of modern semiconductors is to manipulate the topological interface by molecular adsorbates. As an example, we present the high-end recent experimental study of Caputo et al. [41] on this fascinating topic. They performed the study using CoPc and Bi_2Se_3 as prototypical molecules and topological insulators (Tis), respectively, while using angle-resolved photoemission spectroscopy (ARPES) and scanning tunneling microscopy (STM) to probe the electronic structure. A clear downshift of the Dirac cone due to a

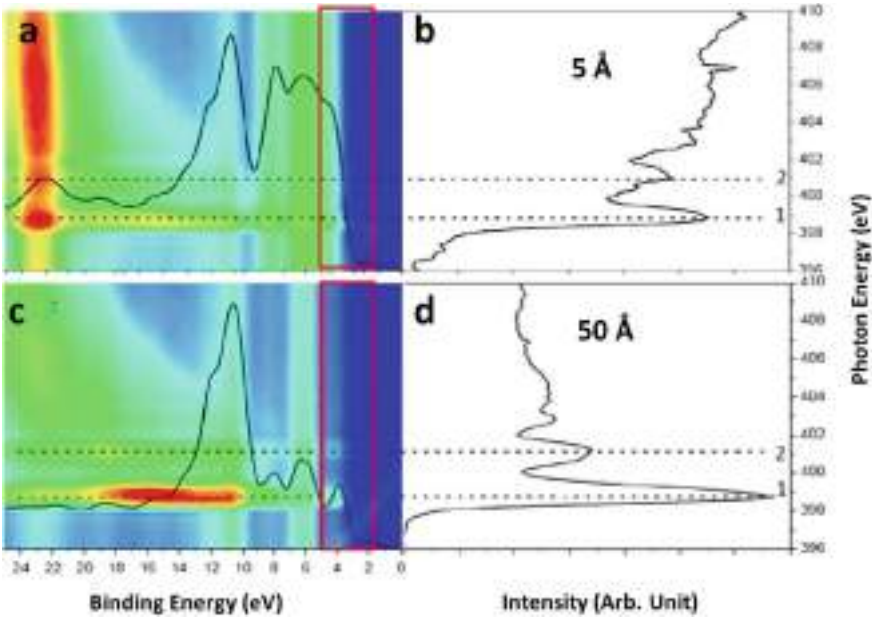

Fig. 7 Contour plots of resonant photoelectron spectra at N-K-edge for **a** 5 Å and **c** 50 Å F_{16} CuPc films on TiO_2. The spectra plotted here are the corresponding valence band measured with photon energy 110 eV. Right panel: the corresponding NEXAFS spectra for **b** 5 Å and **d** 50 Å F_{16}CuPc films on TiO_2 [37]

charge transfer from the molecule to the topological surface is evident for 0.66 ML CoPc/Bi_2Se_3, as shown in Fig. 9. Their results indicate that the existence of a relevant molecule/substrate interaction, with the effect of burying the wave function of the topological surface stage below the first quintuple layer. Therefore, the potential of metalorganic molecules for the control of Dirac fermions in topologically protected states through the metal-metal and the metal-substrate interaction is clearly observed. These outstanding findings can trigger the fundamental research on metalorganic-molecule/topological-insulator interfaces as well as their application in the field of spintronics.

To establish a better understanding of the interfacial energy level alignment, one should not neglect influences related to the structure of organic adsorbate molecules. Planar molecules such as CuPc, rubrene, PTCDI, or pentacene, have negligible dipole moment due to their symmetric planar structures. Distortion arises upon adsorption due to the interaction with the substrate and induced molecular dipoles in the system. Metal phthalocyanine (MPc) can be polar (e.g., chloroaluminum-phthalocyanine (ClAlPc), Vanadyl-phthalocyanine (VOPc)) in addition to the traditional planner non-polar (e.g., CuPc, FePc, ZnPc, etc.) molecules. Non-planar MPc molecules may adsorb in different orientations, form layers with at least partially aligned finite dipole moments. Such polar MPcs open further fields of fundamental studies and device applications [42–45]. In the case of basic studies, one interesting example

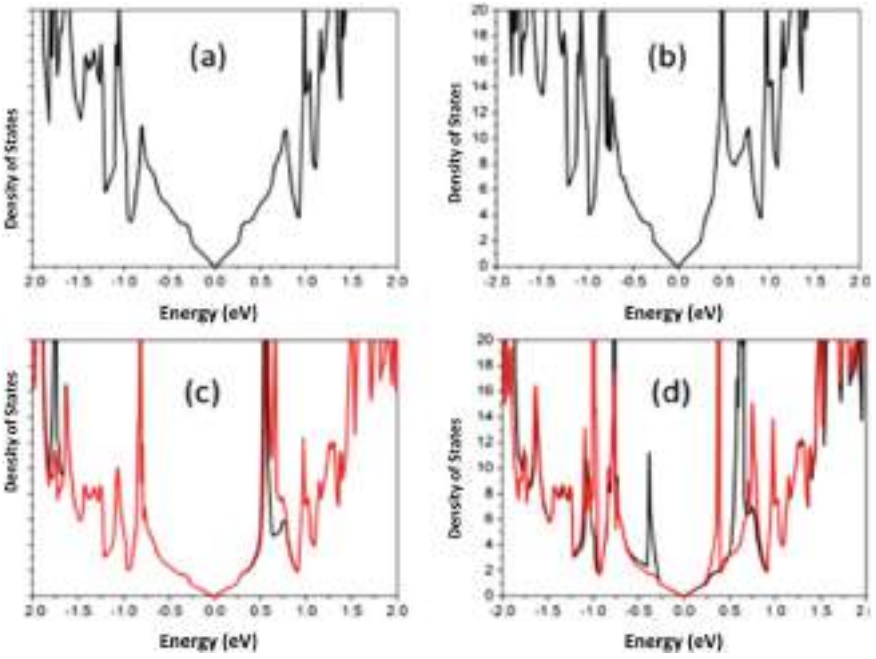

Fig. 8 Total DOS of **a** graphene, **b** SnPc/graphene (Sn-up), **c** CuPc/graphene, and **d** FePc/graphene. The black and the red curves are for the majority spin (spin up) and the minority spin (spin down), respectively. Reprinted from Feng et al. [38], with permission from the American Chemical Society. Copyright (2019)

is the tuning of the interface energetics. The possible dipole-up and dipole-down adsorption configurations of polar phthalocyanines allow tuning of the energy level alignment for the respective interface [42, 43]. Therefore, for this class of systems, the orientational order on the surface is a quantity that strongly affects the interface dipole.

Now, we briefly discuss the recent significant studies on doping of the organic semiconductors. Doping plays a vital role in semiconductor physics. Fermi level control by doping is well-established since several decades in inorganic semiconductors and has been successfully introduced in organic semiconductors. The energy level alignments between hosts and dopants govern several crucial physical processes (such as charge transport and exciton formation) and therefore the performance of organic semiconductor based devices. Hence, design and fabrication of high-end organic devices need a clear understanding of the energy level alignments between hosts and dopants. In 2020, Li and Lu [46] reported their studies on the energy level alignments of various molecular host-dopant systems in doped forms by XPS and UPS spectroscopies. As the host molecules, they selected 4,4′-bis(N-carbazolyl)-1,1′-biphenyl (CBP), N,N′-bis(naphthalen-1-yl)-N,N′-bis(phenyl)benzidine (NPB), and 4,4′-cyclohexylidenebis[N,N-bis(4-methylphenyl)benzenamine] (TAPC). On

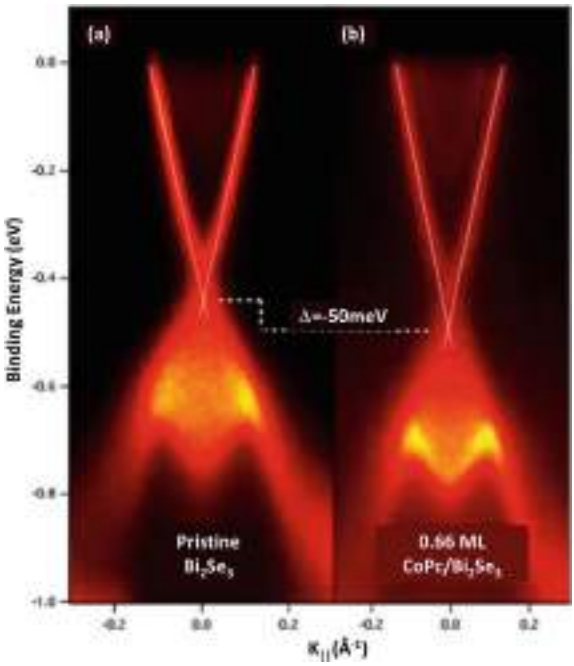

Fig. 9 Enlarged view at the vicinity of the Dirac point for the **a** pristine Bi_2Se_3 surface, and **b** 0.66 ML CoPc/Bi_2Se_3. Reprinted from Caputo et al. [41], with permission from American Chemical Society. Copyright (2016)

the other hand, the dopant molecules were bis[2-(2-pyridinyl-N)phenyl-C](2,4-pentanedionato O^2, O^4)iridium(III) $\left(Ir(ppy)_2(acac)\right)$, tris[1-phenylisoquinoline C^2, N] iridium(III) $\left(Ir(piq)_3\right)$ and bis[2-(2-methylphenyl)-7-methyl-quinoline] (acetylacetonate) iridium(III) ($Ir(dmpq)_2(acac)$). They measured host-dopant HOMO energy offsets from photoelectron spectroscopy and observed that this energy offset is directly related to the detrapping activation energy in charge transport obtained from the electrical characterizations. Moreover, the energy level alignments for host-dopant systems used in light-emitting structures were noticed to fall into the linear elastic region of the universal energy level alignment rule. The energy level alignments in both p-type and n-type doped organic systems were also found to obey this universal rule for organic/organic heterojunction interfaces. In another notable recent study, Gaul and his coworkers [47] simulated and experimentally investigated, with direct photoemission spectroscopies (UPS) and indirect photoemission spectroscopy (IPES), the DOS and the Fermi level position of the C_{60} and ZnPc n-doped with highly efficient benzimidazoline radicals (2-Cyc-DMBI). They mainly focused to study the role of doping-induced gap states, and specifically of the energy difference between the electron affinity of the undoped semiconducting material and the ionization potential of its doped counterpart (Δ_1). It has been explored that this parameter plays a key role in free carriers generation as well as affecting the conductivity of the doped films.

Contact contamination is another crucial issue that plays a substantial role in the charge carrier injection at organic semiconductor/electrode interfaces and their

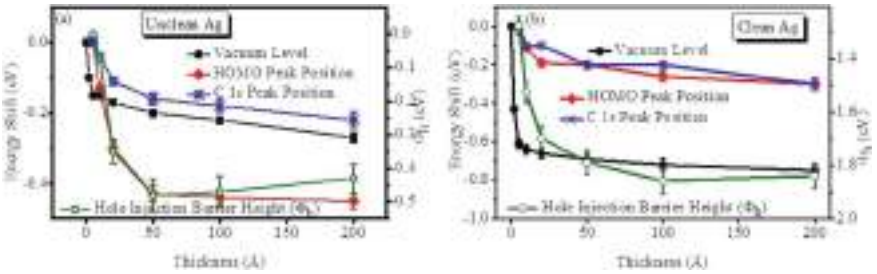

Fig. 10 Binding energy shifts of HOMO as a function of the deposited rubrene film thickness. C 1s peak position and hole injection barrier height (Φ_h) vacuum level of rubrene on **a** unclean, and **b** clean Ag substrates [49]

corresponding interface energetics. Generally, the device fabrication involves the processing of the electrode surfaces either in controlled atmospheres or under ambient conditions; not under UHV conditions. Under those conditions, the molecules of the atmosphere may be adsorbed on the electrode surface, leading to partial oxidation, and/or the passivation of the electrode surface [48]. Here, using XPS and UPS techniques, we discuss the studies about the impact of electrode contaminations on the interfacial energy level alignment at organic semiconductor/noble metal interfaces. The UHV clean Ag and unclean Ag were employed as substrate whereas rubrene was used as organic semiconducting material. The adventitious contamination layer was found to act as a spacer layer between the clean Ag surface and the rubrene layer. It has been also seen that the crucial parameters of the energetics such as C 1s XPS spectra, hole injection barrier height, interface dipole were greatly affected depending on the cleanliness of the Ag substrate, as shown in Fig. 10. The effect of substrate contamination was most at rubrene monolayer, then it was gradual [49].

The contact between the electrode and the organic semiconductor is one of the most crucial factors in determining the organic device performance. Generally, active organic semiconductor layers are sandwiched between two electrodes, in the organic device. We concentrate the investigations carried on the electronic structures at rubrene/Ag and Ag/rubrene interfaces using photoemission spectroscopy. The Ag on rubrene interfaces is found to show more interesting and complex natures than rubrene on Ag substrate. The vacuum level was shifted from push back effect for deposition of rubrene onto Ag film, whereas the electronic features of silver were only suppressed, and no energy shift resulted. While, the deposition of Ag onto rubrene film leads to the diffusion of very small clusters of Ag atoms with quantum size effect, inside the organic film (Fig. 11) [50].

The origin of the inferiority of the performance of organic thin film-based devices than single-crystal ones demands some attention. Among organic molecules, rubrene is a benchmark material for single crystal FET, because field-effect mobility as high as up to about 20 cm^2/V s has been observed [51]. Thin films did not show superior carrier mobilities, spanning from 10^{-6} to 10^{-2} cm^2/V s [52]. Notice that rubrene is a nonplanar molecule comprising of a tetracene backbone core with one pair of

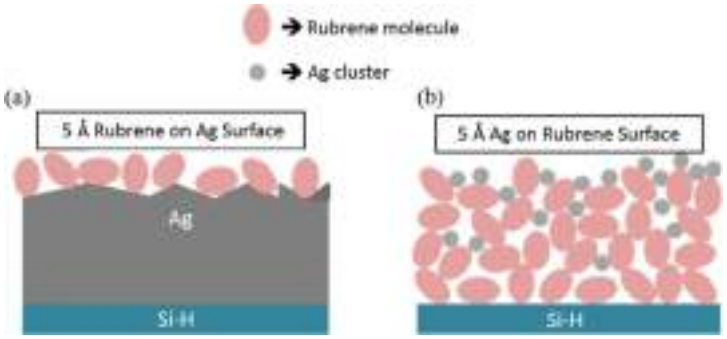

Fig. 11 Schematic representations of interfaces with reverse of deposition sequence of rubrene and Ag **a** rubrene/Ag, and **b** Ag/rubrene interfaces [50]

phenyl substituents attached on either side of the backbone. The intra-molecular steric hindrance between the phenyl side groups results in a significant strain within the molecule which is minimized in two stable configurations. One with a planar tetracene backbone which is seen in the condensed phase geometry. Another configuration is with a twisted backbone observed in the thin film geometry [53]. DFT calculation [54] predicts that the reduction of the HOMO–LUMO gap, as well as the redistribution of the electron density of the HOMO and the LUMO orbitals in case of the twisted molecules and is shown in Fig. 12. This redistribution explains clearly the dropping of conductivity for the twisted molecules than that of the flat ones in spite of the lower HOMO–LUMO gap for the former.

In other works, the family of PTCDI derivative molecules is considered. In this case, several groups of researchers noticed that the mobility of FET significantly

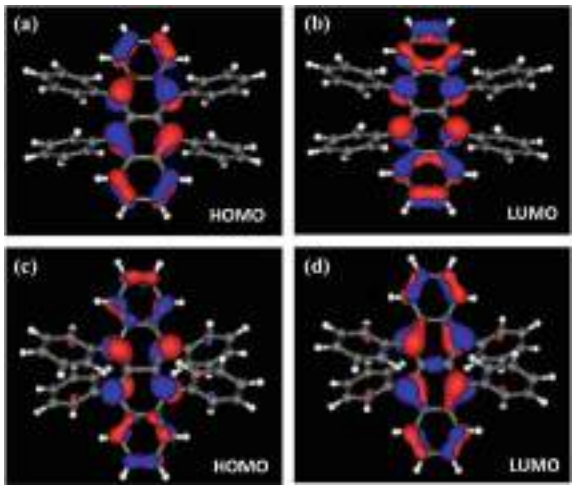

Fig. 12 3D electron density distributions. **a**, **c** HOMO orbitals and **b**, **d** LUMO orbitals of flat and twisted rubrene molecule respectively; white balls represent hydrogen atoms and gray balls represent carbon atoms (corresponding isosurface value $\pm\, 0.04e^{1/2}$ Å$^{-3/2}$). Reprinted from Mukherjee et al. [54], with permission from Royal Society of Chemistry (RSC). Copyright (2018)

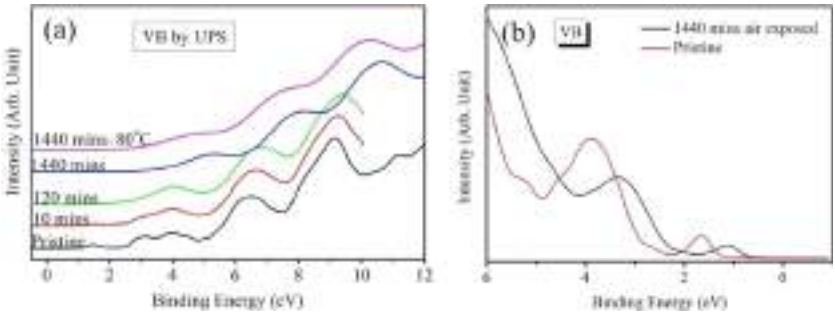

Fig. 13 The valence band (VB) spectra of **a** rubrene, and **b** CuPc thin films before and after ambient environment exposure [58, 59]

changes with the twisting of the perylene cores of the molecules due to the functionalization of the imide nitrogens [55, 56]. These observations can be understood with the findings in the DFT simulated DOS data. DFT calculation explores that the HOMO–LUMO gap is varied with the twisting of the perylene cores. Moreover, the occupied DOS is almost exclusively determined by the chemical structure of the molecule, while the nature of the unoccupied DOS can be significantly affected by physical properties such as molecular twisting [57].

The last but not least issue regarding the wide-spread production of organic electronic devices is the long-term stability in ambient operating conditions. It is a well-known fact that the performance of organic semiconducting thin film-based devices is hampered by the ambient environment. To address this vital point, we will present the finding of the studies on the effects of successive ambient environment exposure to the electronic structures of rubrene and CuPc thin films. It has been shown from theoretical as well as experimental data [58, 59] that the rubrene thin films are more easily degraded by oxidation than CuPc films (Fig. 13). The rubrene was found to convert into rubrene epoxy and rubrene endo-peroxide in ambient exposure, leading to fast oxidation of rubrene thin films. On the other hand, in case of CuPc films, charge carriers were formed due to the adsorption of oxidizing gases in an exposure. The oxygen-induced chemical reaction increased the HOMO–LUMO gap of rubrene thin films, while the gap was decreased for CuPc films [58, 59].

3.3 Optical Properties

The energy gaps of most organic semiconductors lie between 0 and 4 eV. As a consequence, electrons from the filled valence bands can be excited to the empty conduction bands by photons in the optical energy region. Hence, the optical spectra of semiconductors offer a great source of information on their electrical characteristics. Photons can also interact with localized electrons on defects and with lattice

vibrations. Optical techniques are particularly helpful for analyzing these excitations generating from photon-phonon interactions. Their optical properties are the basis of several crucial applications of semiconductors, such as solar cells, light-emitting diodes (LEDs), and photodetectors. The interaction of semiconductors with light plays a key role for optoelectronic and photonic devices as well as for the fundamental characterization of semiconductor properties.

We first take isolated rubrene molecules to discuss the change in the optical properties of a single molecule functionalized by various groups. The calculation of Zhang et al. [60] shows that the maximum absorption wavelengths are red-shifted due to the introduction of cyclopentadienyl or furan groups while those that are blue-shifted due to the substituted methoxy groups on the tetracene backbone. Furthermore, their singlet fission (SF) value, the conversion of one singlet exciton into two triplet excitons, may lead to the realization of high-efficiency organic photovoltaics. Wang et al. [61] has predicted from their theoretical calculation that the triclinic and the monoclinic forms of rubrene will show higher SF efficiencies than the orthorhombic one. Next, we consider the findings from the simulation of various non-planner subphthalocyanine (SubPC) halide derivative molecules (such as, Cl-BsubPc, Cl-AlsubPc, Cl-GasubPc, and Cl-ScsubPc). The static permittivities of these molecules are observed to enhance within the halogen sequence from the calculation, and they are displayed in Fig. 14. The static permittivity directly controls the exciton binding energy, which is crucial for photo-voltaic device performance [62].

In the case of thin films, we first take phthalocyanines as examples. Caplins et al. [63] reported that the effective diffusivity of the singlet and triplet excitons in the α-phase crystal structure of both the H_2Pc and CuPc thin films are fairly different. After that, we discuss the study of optical properties of perylene-3,4,9,10-tetracarboxylic dianhydride (PTCDA) thin films using Ultraviolet-visible (UV–Vis) spectroscopy. The values of refractive index (n) and absorption coefficient (α) of the PTCDA film were found to depend on the film thickness [64]. Baby et al. [65] noticed from their results, obtained using various complementary experimental and theoretical tools that immense geometrical re-orderings occur at the PTCDA/Ag(111) interface upon potassium doping, resulting in enormous modifications of the interfacial electronic

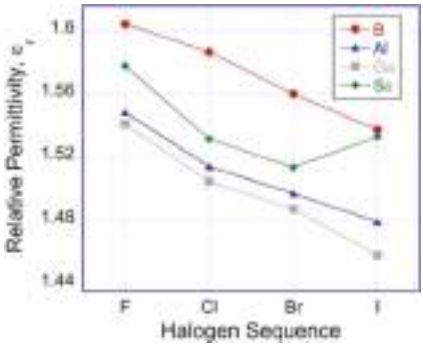

Fig. 14 The static permittivity of the subPC derivatives as a function of chemical substitution. Reprinted from Waters et al. [62], with permission from The Minerals, Metals and Materials Society. Copyright (2019)

and optical properties. The evolution of the optical spectra in terms of frequency-dependent dielectric function (Fig. 15) at intermediate doping levels appears to indicate that the deposited potassium oxidizes rather than further reduces the PTCDA layer. In case of organic doping, it was found that the optical absorption provided a signature of charge transfer (CT) state for tetrafluorotetracyanoquinodimethane (F_4TCNQ)-doped pentacene system in the low-doping limit [66]. In 2017, an interesting theoretical study on the CT states and the optical transitions at the pentacene/TiO_2 interface is reported by Ljungberg et al. [67]. From their *ab initio* calculations they identified that the molecular states appeared within the bandgap of the clean TiO_2 substrate surface. As a result, this allows to directly move the charge-transfer excitations from the molecular HOMO to the TiO_2 conduction band. Moreover, the deduced optical spectrum exhibited a sharp polarization dependence as well as excitonic resonances corresponding to the charge-transfer state (Fig. 16).

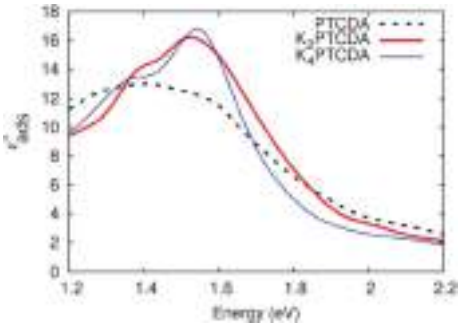

Fig. 15 Imaginary part of the dielectric function for extended PTCDA/Ag(111), K_2PTCDA/Ag(111), and K_4PTCDA/Ag(111) interfaces. Reprinted from Baby et al. [65], under the terms and conditions of the Creative Commons CC-BY license. https://creativecommons.org/licenses/by/4.0/deed.en

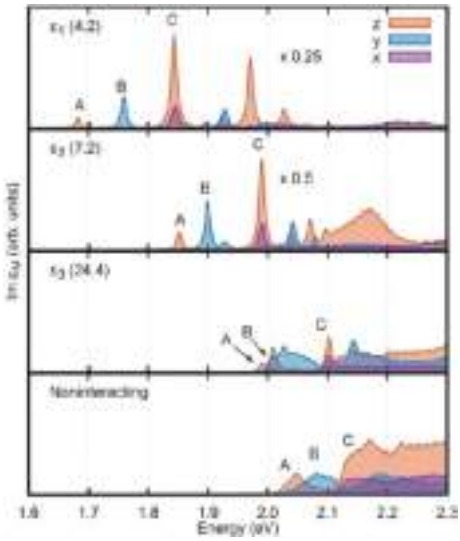

Fig. 16 Macroscopic dielectric function for the pentacene/TiO_2 interface for three polarization directions using different screening parameter values ϵ. The three polarization directions are orange: z-polarization, blue: y-polarization, purple: x-polarization, respectively. Reproduced from Ljungberg et al. [67], under the terms of the Creative Commons Attribution 3.0 license. https://creativecommons.org/licenses/by/3.0/

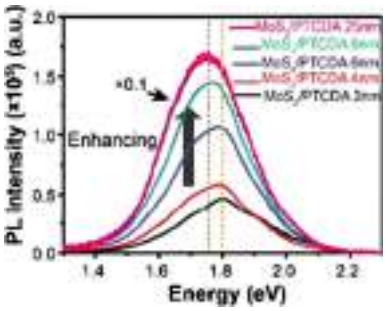

Fig. 17 PL spectra of MoS_2/PTCDA heterostructures with different thickness of the PTCDA films. Reprinted from Habib et al. [68], with permission from Royal Society of Chemistry (RSC). Copyright (2018)

We will now focus on discussing studies of molecular Van der Waal heterojunction. Recently, Habib et al. [68] observed a tunable photoluminescence (PL) spectra with PTCDA layer thickness for MoS_2/PTCDA heterojunctions (Fig. 17). The intensity enhancement as well as peak shift are ascribed to the electron hybridization between the PTCDA film and the MoS_2 monolayer, which is further influenced by the crystalline ordering of the PTCDA film on the MoS_2. Furthermore, in the case of free base phthalocyanine chromophores functionalized MoS_2 nanosheet, they observed from the UV–Vis and PL spectroscopies data that the semiconducting sheets closely interact with these optoelectronically active chromophores [69].

3.4 Applications

In the first two decades of the present century, gigantic growth is observed in the field of research and development of organic semiconductor devices.

3.4.1 Field-Effect Transistors and Sensors

The increasingly impressive electrical performance of modern semiconductors is mostly driving the development of low-power consumption, flexible, light-weight, eco-friendly, and low-cost fabrication of field-effect transistor (FET) devices. The most immediate application area will most likely be in driving elements of active-matrix emissive flat panel displays, large-area sensor arrays, and memory devices. Here, we present substantial recent development of low-weight organic semiconductor based FET and their application as sensors.

Among organic semiconductors, rubrene is one of the benchmark materials because FET based on rubrene single-crystal exhibit the hole mobility as high as 20 cm^2/V s [51]. In 2015, Chang et al. [70] have reported that they have achieved a hole mobility as high as 11.6 $cm^2\ V^{-1}\ s^{-1}$ with rubrene thin-film transistor (TFT) by employing a cumbersome weak epitaxial growth method. While two years later, Fusella et al. [71] fabricated polycrystalline rubrene thin-film based FET with the

grain size of up to 500 μm and recorded mobility as high as 3.5 $cm^2\ V^{-1}\ s^{-1}$ (displayed in Fig. 18). This value is one order of magnitude higher than that of amorphous Si-based TFTs. Moreover, in general, it is noticed that the electrical performance of vacuum evaporated OTFTs and the quality of corresponding thin films immensely depends on underlayer properties, deposition, as well as measurement temperatures, and environmental conditions [72–75]. Among metal phthalocyanines, it is observed that TiOPc, VoPc, CuPc, and F_{16}CuPc are already able to achieve field-effect mobility in the order of 0.1–10 $cm^2\ V^{-1}\ s^{-1}$ using suitable underlayer and deposition temperature [74, 76]. In order to achieve high recovery for a low concentration gas detection tool, Sun et al. [77] fabricated efficient α-6T OTFT based NO_2 gas sensors by varying α-6T film thicknesses and underlayers. Their sensors were able to detect the low concentration of 1 ppm to NO_2 gas and show the rapid recovery of 28 s. Furthermore, Mirza et al. [78] also prepared NO_2 gas sensors to detect sub-ppm level gas using pentacene as an active material. In 2018, Wang et al. [79] first reported multifunctional synaptic transistor based on a MoS_2/PTCDA hybrid heterojunction, with exceptional short-term plasticity (STP) and long-term plasticity (LTP). It shows the flexible tunability of both STP and LTP and synaptic weight changes of up to 60. On the other hand, Dollinger et al. [80] fabricated C_{60} based vertical organic thin-Film transistors with an anodized permeable base. This is currently the fastest organic transistor with a transition frequency of 40 MHz. They also achieved very large transmission factors of 99.9996%. It is very interesting that the researchers even attempted to use organic transistors on paper [81] and OTFT based chemical sensors for wearable bioelectronics [82].

3.4.2 Photovoltaic (PV) Cells, Light-Emitting Diodes (LEDs), and Photodiodes (PDs)

To satisfy the power demands of the world in the present century, it is highly required to develop affordable renewable energy sources. Today, solar or photovoltaic (PV) cells based on organic materials are regarded as promising alternatives to their inorganic counterparts. Some of the advantages of organic PV cells are their lightweight, flexibility, simple processing, and easy tunability of chemical properties of the active organic materials.

It is known for a long-times that the phthalocyanine family has attractive optical properties, we start our discussion on organic PV cells with CuPc, one of the highly studied organic materials. Recently, Ke et al. [83] fabricated efficient fully vacuum-processed planar perovskite solar cells using CuPc as hole selective layers. Their achieved stable best-performing solar cell exhibited a power conversion efficiency (PCE) of 15.42% with an open-circuit voltage (V_{OC}) of 1.04 V and a fill factor (FF) of 77.47%, measured under reverse voltage scanning, and a steady-state efficiency of 14.5%. Torabi et al. [84] also reported a similar study where they additionally varied the deposition temperature of the CuPc hole transporting layer (HTL) to control the PCE of the cell (displayed in Fig. 19). While Kim et al. [85] used N,N′-Di(1-naphthyl)-N, N′-diphenyl-(1,1′-biphenyl)-4, 4′-diamine (NPB) as HTL

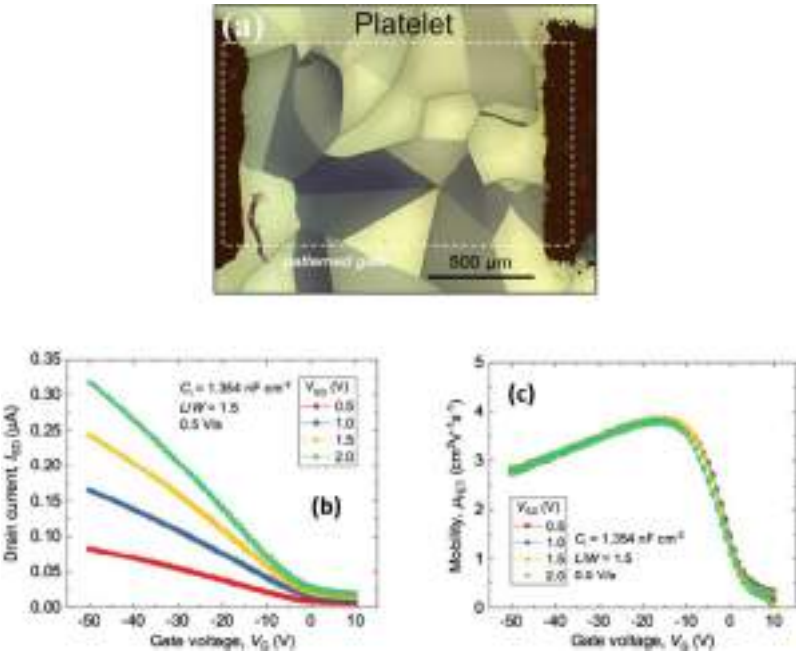

Fig. 18 **a** Polarized optical microscope images for platelet morphology of the rubrene films around the conducting channel, **b** the corresponding plots of the source/drain current (I_{SD}), and **c** FET mobilities in the linear regime (μ_{FET}) as a function of gate voltage (V_G). Reprinted from Fusella et al. [71], with permission from American Chemical Society. Copyright (2017)

material in fully vacuum-processed perovskite solar cells, and recorded V_{OC} as high as 1.12 V, and maximum PCE of 13.7%, due to the effective hole extraction. Yang et al. and his coworkers [86] used pentacene as HTL in the place of conventional Poly(3,4-ethylenedioxythiophene):Poly(styrenesulfonate) (PEDOT:PSS) for planar perovskite solar cells. It is evident from their findings that the pentacene based device shows PCE of 15.90%, which is comparable to that of PEDOT:PSS based one (15.65%). Their fabricated devices also demonstrated relatively high reproducibility of the performance characteristics parameters. The electrons generally move faster than holes in most fullerene-based bulk heterojunction (BHJ) active layers, which results in an unbalanced charge transport and consequently degrades the entire device. To balance the charge transport in inverted organic solar cells, Wang et al. [87] doped high-hole-mobility pentacene in the active layer and observed a light-doping level of 0.2% which significantly improved the PCE of the previous cell by 38%. While Singh et al. used perylene diimide (in place of the conventional electron transporting material, fullerene) based BHJ and were able to achieve highly efficient BHJ solar cells by controlling the molecular geometry and nanoscale morphology of perylene diimide BHJ [88]. Qin et al. [89] prepared a highly efficient perovskite PV cell using

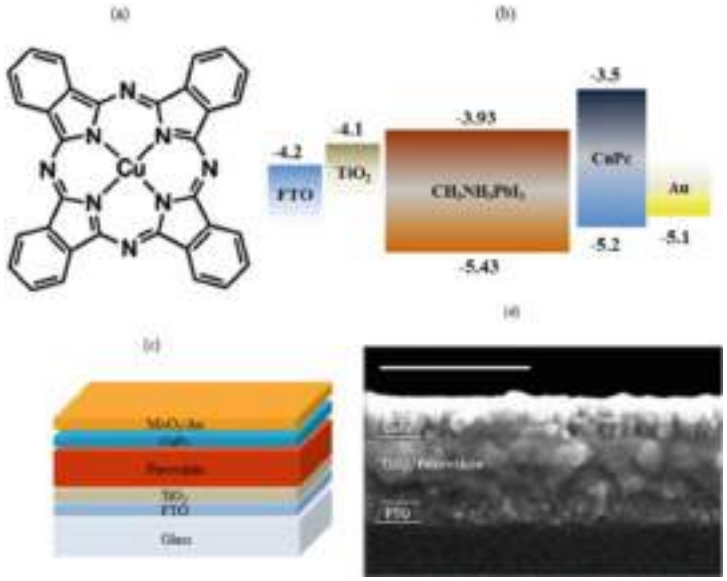

Fig. 19 **a** Schematic diagram of fabricated PV device architecture, and **b** energy level diagram of the corresponding materials used in the device. Reprinted from Torabi et al. [84], with permission from Elsevier. Copyright (2017)

potassium-intercalated rubrene as a dual-functional passivating agent. This material has the ability to suppress the hysteresis, and the corresponding perovskite PV device acquires a high PCE of over 19%, which is higher than that of pristine- and rubrene-based devices.

An exciting research topic in advanced semiconductor devices is photovoltaic FET using 2D-semiconductor/organic-semiconductor van der Waal's hybrid heterostructures. Recently, Park et al. [90] fabricated 2D lateral type n-p heterojunction photovoltaic FETs using MoS_2 as n-type and rubrene as p-type materials. The devices were successfully operated by light irradiation without applying any terminal bias voltage. Jariwala et al. [91] performed a similar study employing pentacene as p-type material, instead of rubrene and they were achieved with reasonable ambipolar high-performance van der Waals hybrid photovoltaic FETs.

The rapid pace of technological growth in organic LEDs (OLEDs) directed toward flat panel display applications, such as laptops, TVs, mobiles, and camera-screen is driven widely by the considerable revenue opportunity in this market segment. For large market penetration, however, active-matrix organic light emitting diode (OLED) display performance should meet or exceed power efficacy, lifetime, color gamut, resolution, and display luminance specifications in order to be competitive with the well-established liquid crystal display (LCD) and plasma display panel (PDP) technologies [92].

Tandem OLED is one which has got significant attention in solid-state lighting due to their high current efficiency, long lifetime, and outstanding stability. In the

year 2017, Liu et al. [93] fabricated efficient blue fluorescent tandem OLEDs based on the charge generation layer (CGL) of C_{60}/rubrene: MoO_3 and the electron injection layer (EIL) of LiF/Al. They observed maximal current efficiency (CE) and power efficiency (PE) of optimal tandem device reach up to 43.1 cd/A and 15.1 lm/W, respectively, which are $\approx$ 2.8 and 1.9 times those of the single-emissive-unit device. The driving voltage of the optimal device is reduced by 6 V and the turn-on voltage is decreased by 2.4 V, compared with the traditional tandem device. On the other hand, Guo et al. [94] reported a study by preparing tandem OLED with pentacene/C_{70} heterojunction as CGL. They achieved the maximum of the values of the CE, PE, and external quantum efficiency (EQE) as 81.8 lm/W, 141.2 cd/W, 38.0%, respectively. Though the scientists have got success in several cases using organic heterojunctions (OHJs) as CGLs in the construction of efficient tandem OLEDs, the charge generation process in the CGLs yet remains unclear. Sun et al. [95] tried to understand this process by fabricating OLED with a typical OHJ CGL composed of 1,4,5,8,9,12-hexaazatriphenylene-hexacarbonitrile(HAT-CN)/4,4′,4″-tris(N-3-methylphenyl-Nphenylamino) triphenylamine (mMTDATA). They found that the charge generation process in this OHJ could be explained in terms of electron tunneling. The maximum power efficiency, current efficiency, and external quantum efficiency of their fabricated tandem device reach as high as 120 lm/W, 201 cd/A and 54.5%, respectively. As per expectation, these values are markedly enhanced compared to those of the corresponding single-unit device. In this field, another interesting topic is the photovoltaic effect on the performance of OLEDs. Zhao et al. [96] introduced a photovoltaic planar heterojunction (PHJ) of C_{60}/CuPc into single light-emitting unit OLED (Fig. 20) to increase the device efficiency. It has been revealed that the photovoltaic effect of PHJ can lead to partial absorption of photons that are radiated from the emission zone, and then producing excitons, leading to free charge generation. As a result, an EL performance was found to enhance from 2275 to 4130 cd/m^2 at a current density of 20 mA/cm^2. Moreover, it is particularly increased with red, green and blue emitting layer. In addition, it can be mentioned here that a lot of researchers have only attracted to develop better OLED design, employing earlier used materials to obtain higher efficient OLEDs [97].

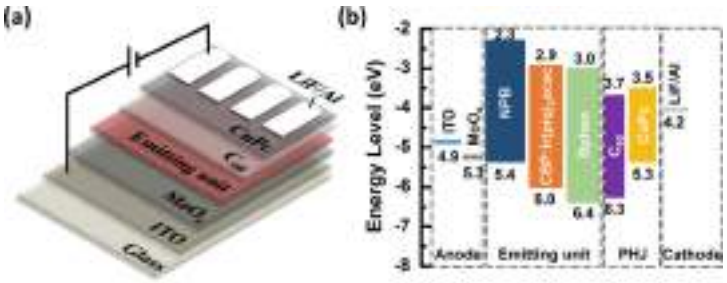

Fig. 20 **a** Schematic illustration of OLED device architecture C_{60}/CuPc photovoltaic PHJ, and **b** energy level diagram of the corresponding materials employed in OLED. Reprinted from Zhao et al. [96], with permission from Elsevier. Copyright (2017)

Next, we focus to discuss photodiodes, another widely used optoelectronic device. Peng et al. [98] fabricated and characterized photodiodes (PDs) based on monolayer MoS_2/pentacene heterojunction. Their most efficient PD with a MoO_3/Au top electrode has shown a high photoresponsivity of 0.31 A/W, EQE of 58.1%, photo-to-dark current ratio of 9.2×10^5, and specific detectivity of 1.55×10^{13} Jones. Furthermore, Joo et al. [99] prepared highly efficient fab-compatible processed near-infrared (NIR) thin-film PD with 3.3×10^{12} Jones detectivity and 80% EQE employing ClInPc: C_{60} thin films as an active layer of the device. Near infra-red organic PDs are so exciting because they are potential candidates for future applications in artificial retinal implants [100]. In 2017, Kim et al. [101] fabricated, an organic vertical p–n junction (p-type pentacene/n-type PTCDI-C8) on top of a graphene electrode comprising a novel gate-tunable PD device structure. This Schottky barrier-controllable graphene electrode boosts the rectification in vertical p-type pentacene/n-type PTCDI-C8 junction photodiodes. Before we conclude our discussion, it is interesting to point out that the researchers have even tried to fabricate printed organic transistors which is a significant development in the field of wearable and disposable sensors [102].

4 Organic–Inorganic Perovskite Semiconductors

4.1 Materials

An alternative approach involves utilizing resonant interactions within organic-inorganic hybrid structures to leverage the unique properties of organic electronic compounds. In these hybrids, the high conductivity of the inorganic semiconductor can be integrated with the organic component's strong light-matter interaction, creating a synergistic effect within the same structure. Ultimately, this is done in the system of organic-inorganic hybrid perovskites. These hybrid semiconductors possess a unique set of attractive optoelectronics characteristics, such as appropriate direct band gap, high light absorption coefficient, low exciton binding energy, absorption high charge carrier mobility, and long intrinsic carrier recombination lifetime, achieving a certified power conversion efficiencies (PCEs) of about 22% with a relatively simple and low-cost route [103].

Perovskite materials are a class of crystalline materials with the formula AMX_3, in which A and M are cations and X represents an anion. The A cation resides at the eight corners of the cubic unit cell, while the B cation is located at the center of the body of an octahedral $[MX_6]^{4-}$ cluster. In organic-inorganic hybrid perovskites, A are monovalent organic cations (methylammonium (MA or $CH_3NH_3^+$) or formamidinium (FA or $(NH_2)_2CH^+$)), M are divalent group IVa cations (Pb_2^+, Sn_2^+), and X are halide anions (I^-, Br^-, Cl^-). The general structure of 3D organic-inorganic hybrid perovskite is shown in Fig. 21 [103–105].

Furthermore, in recent times, a unique type of 2D hybrid perovskite semiconductors, covalently bonded monolayer while few-layer thin film stacked through vdW

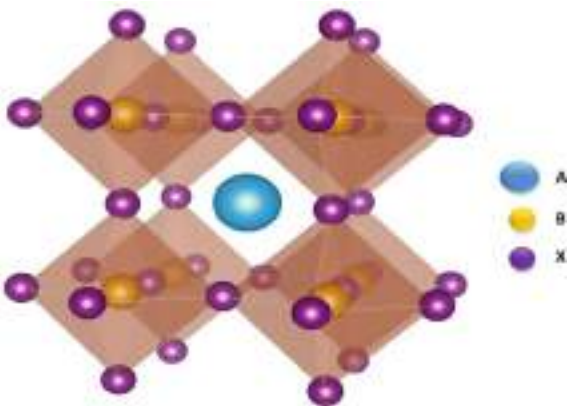

Fig. 21 Illustration of the structure of a 3D AMX_3 organic-inorganic hybrid perovskite. Redrawn by the authors

interaction show intriguing characteristics such as abundant and tunable electronic properties, large specific surface area, exciting optical as well as catalytic properties, and easy for integration. A typical bulk organic-inorganic hybrid perovskite A_2MX_4 (A: organic cation; M: metal cation; X: halide) comprises of organic chains and separated by $[MX_4]^{2-}$ backbone layers. The adjacent layers are weakly bounded via vdW forces. For such a layered structure, it is possible to exfoliate single or few-layer thick 2D sheet of A_2MX_4 from their bulk counterpart [106–108].

The impressive PCE is recorded with lead (Pb) based hybrid perovskites solar cell. But, Pb is toxic to the environment and organisms for a long time and is hard to excrete from the body. Therefore, it is imperative to find environmentally friendly metal ions to replace Pb for the further progress of solar cells as well as other optoelectronic devices. Recent work has shown that Sn, Ge, Cu, Bi, and Sb ions can be used as alternative ions in perovskite configurations to form a new environmentally friendly Pb-free perovskite structure. Particularly, Sn-based hybrid perovskites have very comparable crystal and band structures to lead-based perovskites. In addition, various Sn-based hybrid perovskites are already possible to be synthesized [103–108]. Hence, we concentrate on presenting a brief review on electronic as well as optical properties and device applications of the lower-toxic tin based hybrid perovskites, the most promising candidate among lead-free perovskite materials.

4.2 Electronic Properties

Tao and his co-workers [109] systematically investigated the energy levels of all primary Sn- and Pb-based halide perovskites employing methods of combined photoelectron spectroscopy measurements, DFT calculations, and a tight-binding analysis. Figure 22 displays UPS and IPES spectra of corresponding films of all 18 Sn- and Pb-based AMX_3 perovskites. The ionization energy (IE, position of the VB

maximum), was found to evolve more strongly than the electron affinity (EA, position of the CB maximum) and was understood in terms of the hybridization between the M,s and the X,p states. Overall, they explored that the energy level variations are mainly determined by the relative positions of the atomic energy levels of metal cations and halide anions, and secondarily effected by the strength of the cation-anion interaction. The first-principles calculations [110] were carried out at the level of DFT (Generalized Gradient Approximation (GGA), Heyd–Scuceria–Ernserhof (HSE06), metaGGA, and Tran-Blaha modified Becke–Johnson potential (TB-mBJ) level) to explore the possibility of producing lead free hybrid organic-inorganic perovskites that can be promising for solar cell applications. The study involves the hybrid organic-inorganic perovskites including $CH_3NH_3SnI_3$, $HC(NH_2)_2SnI_3$, $NH_2NH_3SnI_3$, $NH_2(CH_2)_3SnI_3$ in which the first two were experimentally synthesized and the others remain hypothetical. It is interesting to point out that all of them are direct-band gap materials with both valence band maximum (VBM) and conduction band minimum (CBM) located at N, Brillouin zone. The HSE06 calculations on the first two reveal the band gaps of 1.65 eV (Experimental value is in the range 1.23–1.35 eV) and 1.75 eV (Experimental value is 1.41 eV). The last two hypothetical ones are characterized by the HSE06 band gaps of 1.63 eV and 1.80 eV, respectively. The desirable range of band gaps may be obtained by accumulating additional organic cations A and considering larger models.

Recently, in case of tin-iodide perovskites, tunable polarization [111] was observed in the framework of spin orbit coupling based DFT calculations. The Hamiltonian of this noncentrosymmetic $(FA)SnI_3$ contains both Rashbha as well as Dresselhaus types of spin-orbit coupling terms. It was revealed that the spin splittings in the VBM are larger than in the CBM, where they are almost negligible, when

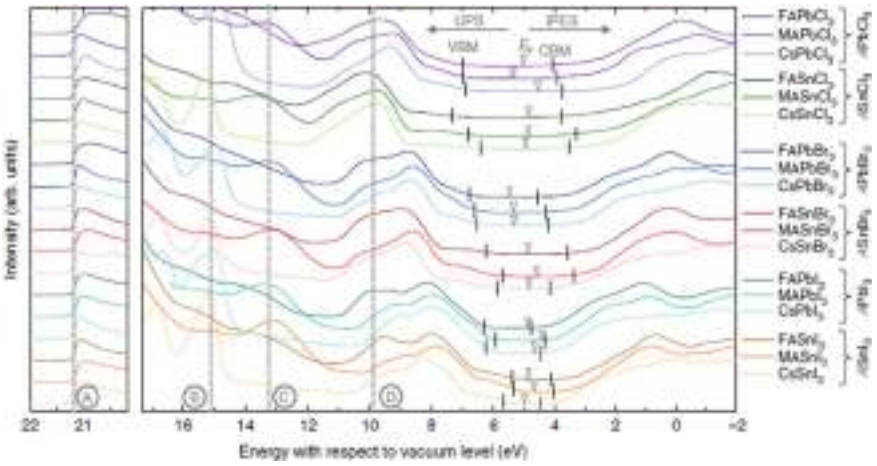

Fig. 22 Representative UPS and IPES spectra of all 18 3D organic metal halide hybrid perovskites. Reproduced from Tao et al. [109], under the terms and conditions of the Creative Commons (CC BY) Attribution 4.0 International License. http://creativecommons.org/licenses/by/4.0/

the polar axis is parallel to [001]. Besides, the Dresselhaus-like spin textures at the CBM are indeed reversed when going from − P to + P in the ferroelectric structure. The energy band gap estimated for $(FA)SnI_3$ based on GW calculations turns out to be 1.07 eV, too small indeed for efficient photovoltaic applications. However, due to the high tunability of the ferroelectric polarization, the (controllable) co-existence of Rashbha and Dresselhaus effects in spin-orbit coupling can provide new ways to exploit the spin degrees of freedom in photovoltaics and important optical properties such as magnetophotocurrent.

It was found from a theoretical calculation that the band gaps of the single-layer 2D hybrid perovskites BA_2MI_4 (M = Ge, Sn, and Pb) lie between 1.5 and 2.0 eV. Moreover, the band gaps of the atomically thin 2D BA_2GeI_4 and BA_2SnI_4 perovskites were calculated as 1.74 and 1.45 eV, respectively. These two particular single-layer 2D hybrid perovskites may be flourished as potential candidates for future lead-free 2D perovskites applications [112].

4.3 Optical Properties

The success of organic hybrid perovskite semiconductors is mainly in the solar cell and LED applications, i.e., in the field of optoeletronics. In this section, we will mostly concentrate on recent significant studies of the optical properties of lower-toxic tin-based hybrid perovskites.

Tuoc and Huan [110] calculated frequency-dependent dielectric function ($\epsilon(\omega)$) and absorption coefficient $a(\omega)$ for a set of four Pb-free hybrid halide perovskites, namely $CH_3NH_3SnI_3$, $HC(NH_2)_2SnI_3$, $NH_2NH_3SnI_3$, and $NH_2(CH_2)_3SnI_3$. Among four studied perovskites, $CH_3NH_3SnI_3$ was found to show notably higher dielectric functions and absorption coefficient. This may be due to the nearly multiple degenerate unoccupied bands at few points. In the case of tin-based hybrid double perovskites ($ABiCuX_6$ [A = Cs_2, $(MA)_2$, $(FA)_2$, CsMA, CsFA, MAFA; X = I, Br, Cl]). Roknuzzaman et al. [113] studied the optical properties using first-principles DFT calculation. It is observed from the simulated band gap values that the variation of band gap with the replacement of halogen atoms is higher in the system of $(FA)_2BiCuX_6$ (X = I, Br, Cl) double perovskites, which covers the entire visible light spectra. This makes them ideal for colored light-emitting diodes. Moreover, the $(FA)_2BiCuI_6$ hybrid double perovskite exhibited high absorption coefficient, promising dielectric properties and high optical conductivity, superior optoelectronic properties to the other considered double perovskites.

Furthermore, for 2D Sn-based perovskite, the researchers observed that 2D $(PEA)_2SnI_4$ perovskite displayed superior photoluminescence properties to conventional 3D $CH_3NH_3SnI_3$ which helped to achieve good LED characteristics [114]. But, the limitation of this $(PEA)_2SnI_4$ perovskite is the oxidation of tin, which leads to instability in device operation. To prevent this oxidation, Yuan et al. [115] added valeric acid (VA) with $(PEA)_2SnI_4$ perovskite and deposited thin films. The $(PEA)_2SnI_4$ films prepared with VA exhibited a narrow excitonic absorption peak

at around 612 nm and a PL emission peak at about 630 nm, which is blue-shifted $\approx$ 10 nm with respect to that of the pristine $(PEA)_2SnI_4$ films, shown in Fig. 23. This small amount of blue-shift of emission peak may arise from the reduced trap emission of VA incorporated $(PEA)_2SnI_4$ films. The quantum yield of $(PEA)_2SnI_4$ films enhanced seven-times from pristine to VA incorporated $(PEA)_2SnI_4$ films. They explained this enhancement of the quantum yield in terms of the reduction of Sn_2^+ vacancies and trap states.

Further, they measured time-resolved PL spectra of $(PEA)_2SnI_4$ films prepared with and without VA to indicate the relevant exciton recombination dynamics and fitted by biexponential decay curves (shown in Fig. 23). From the biexponential decay behavior, they concluded that there are two different time scales involved in the emission. Moreover, they explained that the short-lived PL lifetime is related to surface recombination while the longer lifetime is related to bulk recombination.

4.4 Applications

FETs, Solar Cells, and LEDs

Here, we will briefly discuss the recent major development of lower-toxic tin-based hybrid perovskites, the most promising candidate among lead-free perovskite materials, for FET, solar cell, and LED applications.

2D lead-free hybrid perovskite $(PEA)_2SnI_4$ (PEA: $C_6H_5C_2H_4NH_3$) were used as a material of semiconducting channel of thin film transistor (TFT). In addition, the ferroelectric polymer poly(vinylidene fluoride-trifluoroethylene) (P(VDF-TrFE)) was employed for the dielectric layer. Under polarization "up" and "down" states, the device reached a high photo-switching on/off ratio (> 100) and a short photoresponse time (50 ms), respectively. Moreover, the device also exhibited a high responsivity of 14.57 A/W and a high detectivity of 1.74×10^{-12} Jones under the polarization "up" state with an illumination intensity of 21 mW cm^{-2} [116]. In 2019, Gao et al. [117] synthesized a new stable Sn(II)-based 2D perovskite featuring a π-conjugated oligothiophene ligand, namely $(4Tm)_2SnI_4$, where 4Tm is (3‴,4′-dimethyl-[2,2′:5′,2″:5″,2‴-quaterthiophen]-5-yl)ethan-1-ammonium. They reached hole mobility up to 2.32 $cm^2\ V^{-1}\ s^{-1}$ by fabricating $(4Tm)_2SnI_4$ based thin film FETs and drastically enhanced stability over the earlier benchmark material $(PEA)_2SnI_4$.

Hybrid perovskite-based LEDs are currently approaching the upper limits of EQE, but their application is still limited by reliance on Pb and inadequate color purity. In this scenario, in 2017, Lanzetta and his coworkers [114] fabricated a device using a classical 2D $(PEA)_2SnI_4$ perovskite emitter sandwiched between Indium tin oxide/Poly(3,4-ethylenedioxythiophene):Poly(styrenesulfonate) (ITO/PEDOT:PSS) and F_8/LiF/Al hole and electron injection electrodes, respectively. Their LED achieves a luminance of 0.15 cd/m^2 at 4.7 mA/cm^2 and an efficacy of 0.029 cd/A at 3.6 V. In 2020, Yuan [115] reported high-efficiency valeric acid (VA) incorporated $(PEA)_2SnI_4$perovskite LEDs with color coordinates (0.708, 0.292) that

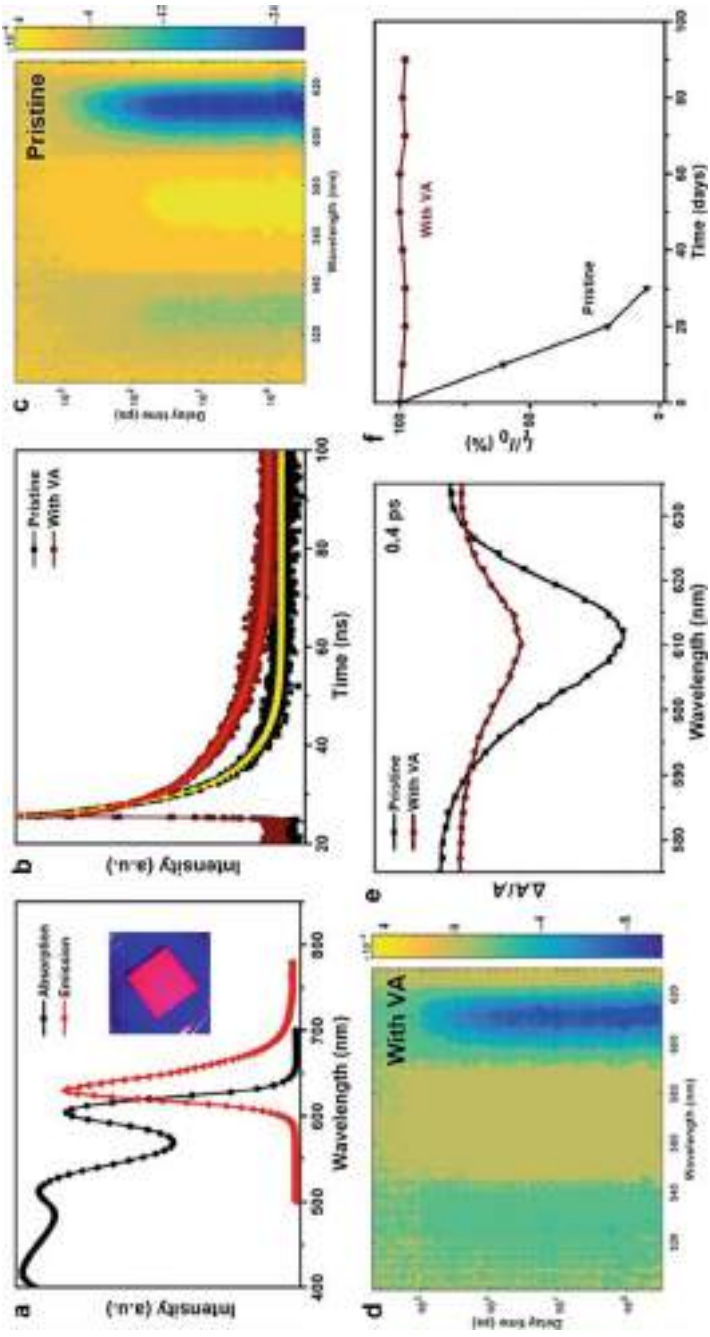

Fig. 23 **a** Absorption and PL spectra of PEA_2SnI_4. The inset displays the image of light emission under excitation of UV light. **b** Time-resolved PL and corresponding fits of pristine PEA_2SnI_4 films produced with and without VA. 2D pseudocolor map of fs-TA spectra of pristine PEA_2SnI_4 films **c** without VA, and **d** with VA, expressed as a function of both delay time and probe wavelength. **e** TA signal of pristine films at 612 nm with an excitation wavelength of 650 nm and delay time of 0.4 ps. **f** Normalized emission intensity of PEA_2SnI_4 films prepared with and without VA after storing for 3 months. Reproduced from Yuan et al. [115], under the terms of the Creative Commons Attribution NonCommercial License 4.0 (CC BY-NC). https://creativecommons.org/licenses/by-nc/4.0/

fulfill the specification for market available red emitters. The incorporation of VA protected tin from undesired oxidation during the film growing process, slowed the perovskite crystallization rate, and also improved the film morphology. The VA incorporated exhibited an EQE of 5% and an operating half-life was more than 15 h at an initial brightness of 20 cd/m^2. Similarly, to suppress the oxidation of tin, Liang and his coworkers [118] used H_3PO_2 which mainly increased the energetic barrier toward Sn oxidation. The H_3PO_2 also improves the film quality by additionally seeded crystal growth during film formation. They reported that their optimized Sn-based perovskite LEDs exhibited a maximum luminance of 70 cd/m^2 under 5.8 V and reached an EQE of 0.3%.

Now, let us switch on to the discussion of the non-toxic tin based hybrid perovskites for solar cell applications. They are already considered as probable lower toxicity alternates for PV cell applications. But, the efficiency of Sn-based perovskite solar cells is still low and they show poor stability in air. In 2017, Ke et al. [119] have reported that they were able to significantly improve Sn-based solar cells performance and stability using "hollow" ethylenediammonium (en) and methylammonium tin iodide (enMASnI_3) perovskite as absorbers. The cation (en) incorporated M$ASnI_3$ perovskite exhibited major changes in the optoelectronic properties without any modification in structure type. The best-performing enM$ASnI_3$ PV cell reached a PCE of 6.63% with an open circuit voltage of 428.67 mV, a short-circuit current density of 24.28 mA cm^{-2}, and a fill factor of 63.72%. In addition, the enM$ASnI_3$ PV device demonstrated better air stability than their neat M$ASnI_3$ counterpart. Similar to enF$ASnI_3$, the (en) becomes a di-cation and enters the M$ASnI_3$ crystal structure without lowering the dimensionality to 2D. The achieved highest PCE for enF$ASnI_3$ solar cells is 7.14% [120]. Moreover, recent findings have reported planar cells with promising results based on (FA)(MA)SnI_3 with 8.12% PCE [121]. To solve this vital issue of air stability, Chen and his coworkers [122] made a recent attempt by incorporating a large divalent organic cation, 4-(aminomethyl)piperidinium (4AMP), in F$ASnI_3$ thin films. This incorporation successfully helped to improve stability, optoelectronic properties, and PV performance. Their optimized PV cells achieved a maximum PCE of 10.9%, and good 500-h operational stability under continuous illumination.

5 Two-Dimensional (2D) Semiconductors

5.1 Materials

Two-dimensional (2D) semiconductors are budding as emerging materials for a broad range of applications in electronics, optoelectronics, spintronics, valleytronics, and catalysis [4]. An inventory of several 2D semiconductor families studied as yet is displayed in Fig. 24 with their crystal structures and bandgap values. The benchmark

discovery of graphene by Novoselov et al. in 2004 [123] not only led to the emergence as well as the progress of a highly encouraging scientific field, but also the difficulty in reliably opening a band gap in graphene has triggered to the search for alternative 2D semiconducting materials [124–126]. To serve this purpose, monolayer and few-layers of the semi-metallic (group IV) materials such as silicene (Si) [127, 128], germanene (Ge) [129], stanene (Sn), etc., and the semiconducting (group V) elements of phosphorene (P), arsenene (As) 2D elemental materials potentially find their applications in flexible, transparent electronics and optoelectronics devices [130].

However, it also stimulated the growth of a wider scientific area of research and applications of 2D semiconductors beyond elemental materials, such as hexagonal boron nitride (h-BN), transition-metal dichalcogenides (TMDCs), layered elemental materials (e.g., black phosphorus (BP), silicene, etc.), layered monochalcogenides (e.g., SnS, GeS, GeSe, etc.)/trichalcogenides (e.g., HfS_3, TiS_3, Bi_2T_3, etc.), and van der Waals (vdW) heterostructures [131–134].

The 2D semiconductors are layered materials showing strong in-plane covalent bonding and weak vdWs intra-plane bonding, which permit them to be easily cleaved into stable atomically thin materials. The 2D semiconductors are also observed as both p-type and n-type. MoS_2, $MoTe_2$, WS_2, etc. are the typical examples of n-type, whereas $MoSe_2$, and WSe_2 are p-type 2D semiconductors [134].

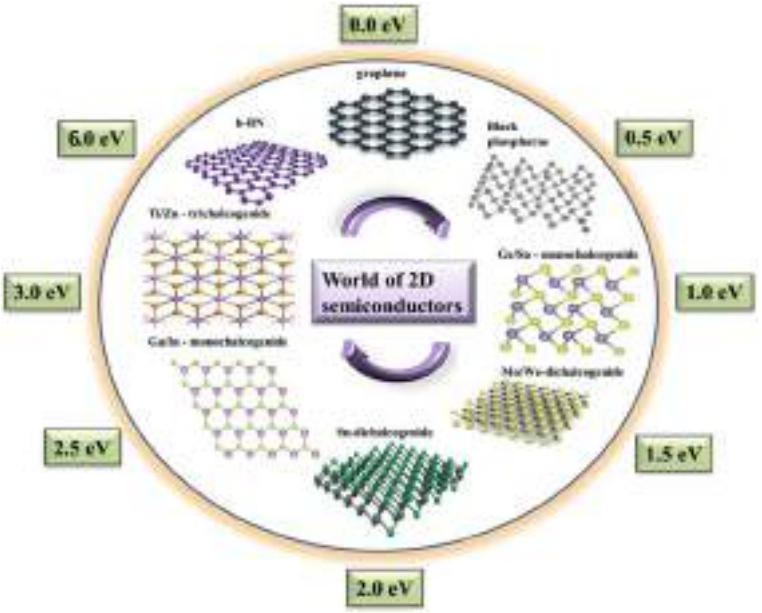

Fig. 24 A catalogue of various 2D semiconductors families with their crystal structure and band gap

5.2 Electronics Properties

As the electronic properties are pivotal to any semiconductor, this is of particular importance in the case of 2D materials. Apart from semi-metallic graphene and indirect semiconducting h-BN (band gap 4.3 eV), free standing silicene, germanene and stanene share several interesting electronic properties [135, 136]. Group IV 2D crystals have half-filled bands derived from p_z orbitals which, under inversion symmetry, give Dirac points (the contact point of the VB maxima and CB minima) at the highly symmetric positions of the Brillouin zone [137, 138]. Spin-orbit coupling (SOC) can open a band gap of 73.5, 23.9 and 1.55 meV for stanene, germanene and silicene, respectively, at the otherwise gapless Dirac points. Besides the weak SOC effect, the application of external electric field, vacancy and hydrogenation of these supported crystals may rise to wide band gap properties, useful for optoelectronics [139, 140]. On the other hand, group-V elements such as phosphorene, antimonene, and arsenene are known to be semiconductors in their pristine form. All the polymorphs of phosphorene are semiconductors with band gap ranging from 0.4 to 2.1 eV [141]. The various structures of arsenene are also predicted to be semiconductors with band gap varying from 1 to 2.5 eV [142]. Again the monolayer of antimonene has an indirect band gap of 2.28 eV which decreases with the increase of the number of layers [143]. This reflects the fact that elements in group V have one more valence electron than those in group IV, so that the half-filled π bands of the group-IV 2D crystals are now filled. Compared to the two conventional 2D materials, such as graphene and other TMDCs, black phosphorene (BP) is a comprehensively dominant choice for 2D electronic devices because of its high charge-carrier mobility and current-switching ratio.

With the thriving progress in elemental 2D materials, recent research has been focused on a family of metallic and semiconducting TMDCs [144]. Out of approximately 40 TMDCs, some are metallic (e.g., VS_2 and NbS_2) and several others are semiconducting (e.g., MoS_2 and WS_2) or insulating (e.g., HfS_2). These properties have been studied experimentally or predicted to be stable theoretically [145]. Semiconducting TMDCs have received significant attention due to their tunable band gap and optical properties. In particular, group-VI monolayer TMDCs are direct gap semiconductors, while their bilayers and thicker multilayers exhibit an indirect gap. For example, MoS_2, $MoSe_2$, WS_2, and WSe_2 all undergo a transition from indirect to direct gap when going from bilayer to monolayer. The band gaps of monolayer TMDCs are in the 1–2 eV range as shown in Fig. 25, ideal for optoelectronic applications. This band gap can be experimentally shown using angle-resolved photoemission spectroscopy (ARPES). ARPES is a crucial experimental tool to study the electronic structures of TMDCs. As an example, ARPES has helped in systematic mapping out the band structures with precise spatial and spin information. The studies of band structure evolution with varying thickness and chemical composition out of various TMDC materials have been carried out using this method. The unusual thickness-dependent band structure of TMDCs can be attributed due to their quantum confinement effect. The gradual evolution of the ARPES data of MoS_2,

on the valence band (Fig. 26) provides direct evidence of band maximum shifting from Γ to K point of the Brillouin zone. This in turn leads to the indirect-to-direct bandgap transition when the thickness is trimmed to monolayer [146]. The band gap also increases with increasing the size of the chalcogen atom, and on the other hand is less sensitive to the size of the transition metal. The valence band maximum (VBM) and conduction band minimum (CBM) are and are mostly contributed by the d orbitals of the transition metal atom which are located at the symmetric corner (K point) of the hexagonal Brillouin zone (BZ). As depicted in Fig. 27, the collection of ARPES spectra reveal the increase in splitting of the local VBM at the K points with the atomic mass by substituting W for Mo, or Se for S. MoS_2 has a splitting of ≈ 0.18 eV; WS_2 has a splitting of ≈ 0.47 eV; and the splitting of WSe_2 local VBM is ≈ 0.5 eV, owing to the increased atomic spin-orbit coupling [147].

The carrier mobility of these materials are nearly 200 $cm^2\ V^{-1}\ s^{-1}$ at room temperature, which enables faster switching time in field effect transistors [148]. The effect of temperature, doping, and defects on the band structure of 2D-TMDCs are very important for electronic and optoelectronic applications. The doped and layered TMDCs also show better carrier mobility than monolayers. The transition metals in TMDCs adopt + 4 oxidation state and the chalcogens − 2 state. This mixed oxidation states produces charged defects which are electronically active. As an example, single vacancies in MoS_2 lead to strong n-type doping. Additionally, these vacancies produce defect states in the mid gap region that are highly localized.

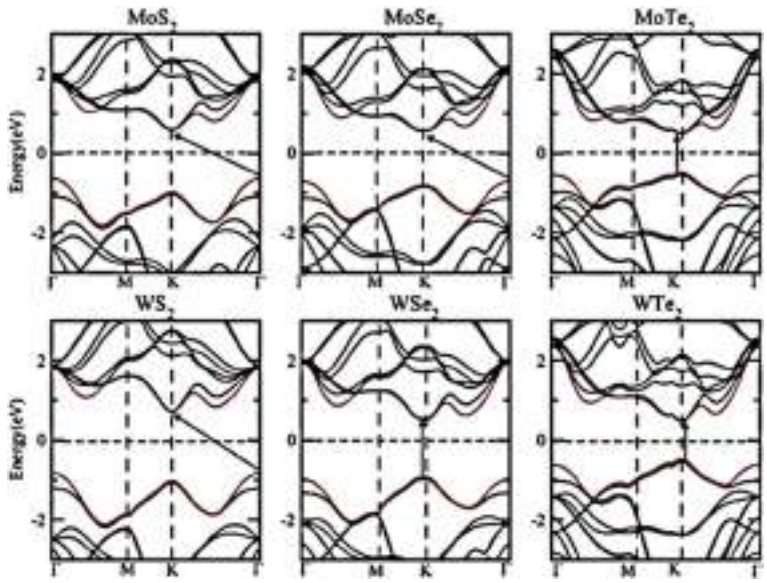

Fig. 25 Electronic band structures of pristine semiconducting TMDCs using DFT calculations. The band gap transitions are also shown. Reprinted from Kumar and Ahluwalia [145], with permission from the Materials Research Society. Copyright (2015)

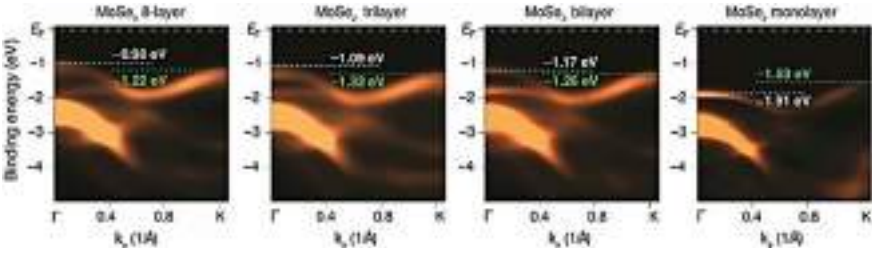

Fig. 26 Layer dependent ARPES spectra of $MoSe_2$ thin films along the Γ–K direction in the BZ. White and green dotted lines indicate the positions of the valence bands apex at the Γ and K points, respectively. Reproduced from Jing et al. [146], under the terms of the Creative Commons Attribution (CC BY 4.0) International License. https://creativecommons.org/licenses/by/4.0/

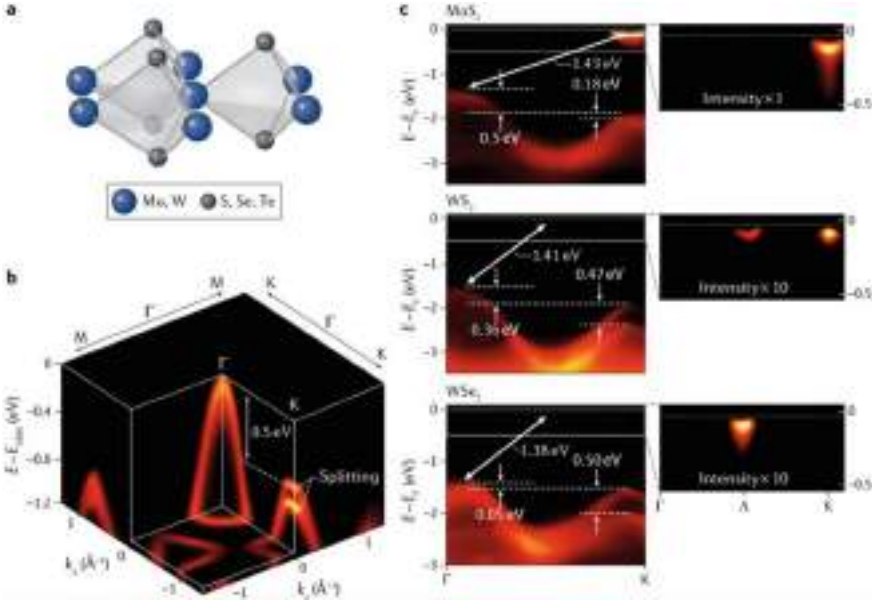

Fig. 27 ARPES studies of transition metal dichalcogenides. **a** Crystal structure of $2H - MX_2$ (M = Mo, W; X = S, Se, Te). **b** ARPES measurements revealing the band structure of bulk MoS_2 with band splitting at the K point. **c** The band spectra along the Γ–K direction for MoS_2, WS_2, and WSe_2, where E is the energy and E_F is the Fermi level. Reprinted from Yang et al. [147], with permission from Springer Nature. Copyright (2018)

Charge transport in MoS_2 occurs through both the localized states and electronic bands which increases the carrier concentration and electrical conductivity. Also the controlled doping techniques in TMDC shifts the device threshold voltages to greater negative potential for n-type doping and that to greater positive side for p-type doping. Thus, the decrease in contact resistances promotes in more charge carrier injection and collection as well. This on the other hand increases the current and

mobility of the carriers [149]. Khan et al. [150] have performed a detailed first-principles study to evaluate the electronic properties of 2D TMDCs in presence of vacancy defects. Three types of defects have been considered in the MX_2 type TMDCs: (i) X vacancy, (ii) X_2 vacancy, and (iii) M vacancy. It was proved that vacancies in the 2D system lead to localized defect states in the band structure. This in turn gives rise to sharp transitions in the in-plane and out-of-plane optical susceptibilities. The spin-orbit coupling induced splitting in these vacancy induced systems is directly related to the atomic number of the transition metal atoms. Among all the considered TMDCs, MoX_2 and WX_2 show the largest splitting energy values. Spin-orbit coupling in TMDCs splits the valence band maximum into two states. The K-point spin degeneracy at the VBM of monolayer TMDC is lifted by SOC, while the degeneracy at the conduction band is conserved. The splitting of valence band energy in monolayer MoS_2 and $MoSe_2$ is predicted to be 160 and 180 meV, respectively.

Xu et al. [151] showed that the vdW stacked MX_2 TMDCs (M = Mo, W; X = S, Se, Te) heterostructures formed by two individual MX_2 monolayers possessing both direct and indirect band-gaps. For this kind of structure, since CBM and VBM reside in two separate monolayers, the electron–hole pairs are spatially separated, which may lead to bound excitons with extended lifetimes and condensation. The single layers in 2D TMDCs are much thinner than the Debye screening lengths. Due to the quantum confinement effect, band engineering in these materials favor the tuning of the band gap to achieve high mobility. This feature is very useful in efficient two-dimensional lasers, light-emitting diodes, and photovoltaic devices.

The energy gap of most of the semiconductors (except for the lead chalcogenides—PbS, PbSe, and PbTe) is known to decrease with increase in temperature. This is due to the electron-phonon interactions and the relative shift in the HOMO and LUMO bands in the semiconductor. The dependency of the energy-gaps on the temperature is given by:

$$E_g(T) = E_g(0) - S\langle\hbar\omega\rangle\left[\coth\left(\frac{\langle\hbar\omega\rangle}{2k_BT}\right) - 1\right], \tag{4}$$

where $E_g(0)$ is the band gap at temperature 0 K, S is the dimensionless coupling constant, k_B is the Boltzmann constant and $\langle\hbar\omega\rangle$ is the average phonon energy. The temperature dependence of the energy gaps of monolayer TMDCs is shown in Fig. 28 [152]. According to this figure, the energy gap decreases with increase in temperature, which is the general behavior for most of the semiconductors. According to Johari et al. [153] strain engineering in TMDCs also gives following significant results. Due to structural composition and stability, a much smaller amount of strain is capable of varying the band gap of TMDC layers compared to that of graphene. An direct-to-indirect band gap and a semiconductor-to-metal transition can be tailored by reducing the mechanical strain in TMDCs.

Depending on its thickness, BP has narrow bandgaps that range from 0.3 eV for bulk to 1.5 eV for monolayer. This bridges the spectral gap between zero-gap graphene and comparatively broad gap TMDCs. Furthermore, BP exhibits an inherent

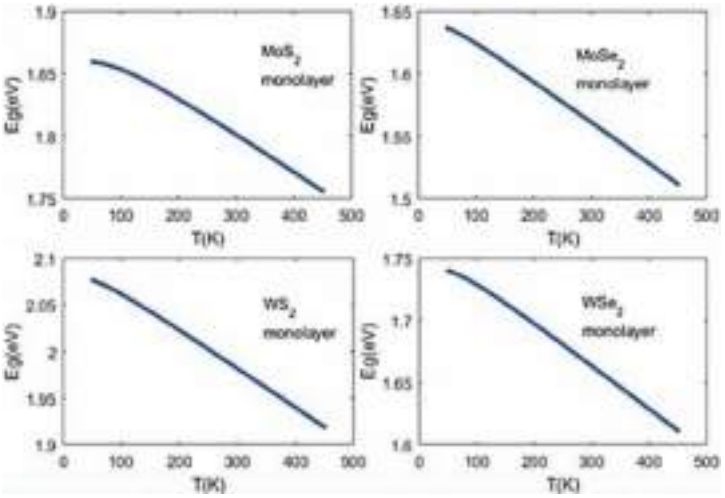

Fig. 28 Temperature variation of the band gap of various transition metal dichalcogenides (TMDCs), calculated using Eq. (1). Reproduced from Tang et al. [152], under the terms of the Creative Commons Attribution 4.0 (CC BY 4.0) International License. https://creativecommons.org/licenses/by/4.0/

direct-gap characteristic independent of the number of layers, opening up possible uses in infrared light emission and detection applications.

The MX (M = Ge, Sn; X = S, Se, Te) monolayers have the same structure as black phosphorene (BP) and can be obtained from the latter by replacing phosphorus atoms alternatively with a group-IV atom and a chalcogen atom. The GeSe monolayer is a direct-band-gap semiconductor [154]. It is noted that the band gaps of the MXs vary over a wide energy range, from 1.01 to 2.74 eV. Apart from all these systems metal phosphorus trichalcogenides MPX_3 and metal vanadium trichalcogenides MVX_3 with M = V, Cr, Mn, Fe, Co, Ni, Cu, Zn and X = S, Se, Te show various metallic, semiconducting behavior depending on their magnetic (ferromagnetic, antiferromagnetic and non-magnetic, etc.) states [155]. These materials open the possibility of various device modulation for high-efficiency electronic devices beyond any physical limits.

5.3 Optical Properties

The world of 2D materials, such as graphene, TMDCs, BP, h-BN, perovskites, topological insulators (Tis), and their hybrid structures, display unique and diverse nonlinear optical response. The optical nonlinearity is a particular characteristics of the concerned materials which can be used for specific photonic applications. Graphene, silicene, germanene, and other widely studied materials show their

nonlinear properties within the broadband absorption at terahertz (THz) frequencies. This is the result of their nearly zero band-gap nature. Graphene-based materials such as graphene oxide and graphene-metal hybrids exhibit strong nonlinear refraction index for a wide range of energies [156]. Although a single layer of graphene appears to be visually transparent, it is an excellent visible light absorber, achieving 2.3% visible light absorbance in just 3 Å thickness [157].

As explained in the previous section, semiconducting properties of 2D TMDC materials have shown unique band and transition properties, depending on the number of layers. When interacting with photons, the radiative recombination, specifically the photon lifetime, is an important property to study for semiconductor TMDCs. Studies have indicated [158] that the exciton radiative lifetime of monolayer TMDCs are in the picosecond (1–10) ps range for low temperature (0–4) K, and in the nanosecond (0.1–10) ns range for the room-temperature decay. It has also been found that the radiative recombination in bulk and few-layers has smaller lifetime than the monolayer TMDCs. In a study by Kumar et al. [159], excitonic dynamics analysis on $MoSe_2$ monolayers and bulk materials, exhibits a decay rate of about 0.9 ns. These authors have also noticed that the bulk form has a decay time about twice as small as the monolayer form. This adds another degree of freedom in optoelectronic capabilities, as the exciton dynamics could be controlled and tuned for various applications.

The optical absorption that takes place when a 2D semiconductor is illuminated with photon energy greater than its band gap. In contrast, photoluminescence (PL) is produced when electron and hole pairs relax to the band boundaries and then recombine by releasing photons with energy equal to the band gap. Several monolayers of TMDCs have shown much higher absorbance at band gap resonances, which usually fall in the visible and near infrared (NIR) range. Absorbance up to > 10% has been observed at excitonic resonances, and even higher for some shorter wavelengths, due to inter-band transitions [160]. Bernardi et al. reported that the absorbance of three different TMDC monolayers (MoS_2, $MoSe_2$, WS_2) for the photon energy of (1.5–2.5) eV. Moreover, it was found that all three TMDCs exhibit absorbance of up to 10% in some parts of the visible spectrum, as well as over 30% absorbance of light for $MoSe_2$ at energies over 2.4 eV, despite all of them being less than 1 nm thick [161]. As an experimental evidence in Fig. 29, the UV-visible absorption spectra of the TMDC, and graphene dispersions typically show characteristic absorption peaks of MoS_2, $MoSe_2$, WS_2, WSe_2 within the region of (500–900) nm [162]. The maximum absorptance (A) for MoS_2, $MoSe_2$, WS_2, and WSe_2 on silicon substrates are 98.81% (1.58 eV), 98.2% (1.61 eV), 99.92% and 99.84% (1.73 eV), respectively, as obtained from peak positions. These values are definitely greater than those of the bulk systems.

Photoluminescence (PL) measurements are usually used to determine the thickness as well as optical properties of TMDCs. The quantum confinement effect in TMDC monolayer results in band repulsion and localization, thereby making it optically more active. Molybdenum dichalcogenides, which include MoS_2, $MoSe_2$, and $MoTe_2$, have shown strong PL properties with PL emission efficiency, up to over 1000 times higher than their bulk forms in the visible and NIR regions [163]. For

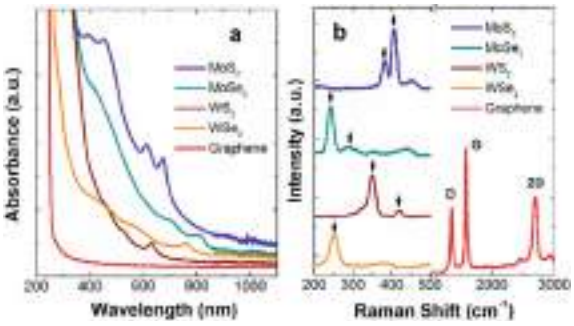

Fig. 29 **a** UV–VIS absorption spectra the TMDC (MoS_2, $MoSe_2$, WS_2 and WSe_2) and graphene dispersions. **b** Raman spectra of the dried TMDC and graphene films. TMDC: MoS_2, $MoSe_2$, WS_2 and WSe_2. Reproduced from Dong et al. [162], under the Creative Commons Attribution 4.0 International CC BY License. http://creativecommons.org/licenses/by/4.0/

Tungsten dichalcogenides, consisting of WS_2, WSe_2 are both semiconductors in both bulk and monolayer form. The indirect optical band gaps of these materials are very similar, with values of about 1.2–1.3 eV [164–166]. As shown in Fig. 30, the measured PL profile for 1–5 layers of these materials show vary small changes in the range (0.2–0.6) eV. 2D TMDCs are direct-band gap semiconductors and have inversion symmetry breaking, thus possessing intriguing PL and second harmonic generation properties in the visible wavelength range. Furthermore, photonsensitive TMDCs can convert visible light into hot carriers, facilitating their application as ultrathin photodetectors and photovoltaic cells [167].

The heterostructures formed by the combination of two different vdW monolayers such as; MoS_2/ZnO, WS_2/ZnO, $MoSe_2$/ZnO, and WSe_2/ZnO show interesting optical properties. All the heterostructures show good ability to absorb light in the visible and near-infrared (NIR) regions [151, 168]. The high absorption peaks are approximately located at 488, 555, 441, and 498 nm in the visible region of their respective spectra. Since the wavelengths of light arriving at the earth are mainly in the visible and NIR regions, these heterostructures are promising components for various optical, photovoltaic and photocatalytic applications. Zhang et al. [169] showed that along with the single TMDC compounds, alloys such as $Mo_xW_{1-x}S_2$, $Mo_xW_{1-x}Se_2$, and $MoS_{2x}Se_{2(1-x)}$ have also been fabricated for specific PL tuning capabilities. By changing the composition of the monolayer material, continuous shift in PL emission peaks can be shown for $MoWSe_2$ in Fig. 31.

As mentioned above, anisotropic 2D semiconductors exhibit intriguing optical properties. For instance, monolayer BP presents a strong angular polarization dependence of relative optical extinction and PL quantum yield [170]. Due to its comparatively high mobility, nano-patterned BP, like graphene, can enable localized plasmonic resonance [171]. One distinctive feature is that the anisotropy of BP causes a strong polarization dependence in the localized plasmonic effect [172]. The appealing spectral coverage of the band gaps, ranging from the ultraviolet to the infrared, diversifies 2D semiconductor family. Through material selection and structure designing

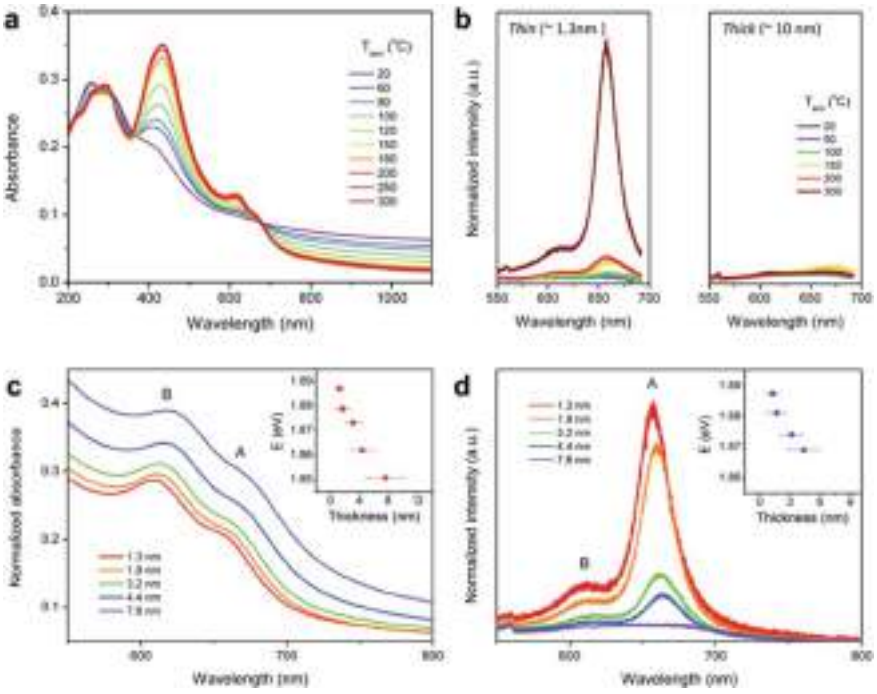

Fig. 30 **a** Absorption and **b** photoluminescence spectra of MoS_2 thin films annealed at several temperatures. **c** Absorption and **d** photoluminescence spectra of MoS_2 thin films of various thicknesses. Reproduced from Bernardi et al. [167] under the Creative Commons Attribution 4.0 International CC BY License. http://creativecommons.org/licenses/by/4.0/

of 2D semiconductors, various optoelectronic applications can be achieved in a certain spectral range.

5.4 Applications

5.4.1 Field-Effect Transistors and Sensors

As it is expected that FETs of 2D semiconductors benefit from their ultrathin body, and exhibit better electrostatics and reduced short-channel effects toward further scaling. In the case of 2D semiconductors, Xu recently introduced [173] a MoS_2- or ReS_2-based back-gate transistor scheme fabricated onto Al_2O_3/ITO/SiO_2/Si stack, as shown in Fig. 32. Both transistors exhibit outstanding electrical characteristics, including steep subthreshold swing (62 μm dec^{-1} for MoS_2 and 83 μm dec^{-1} for ReS_2), high mobility (61.79 cm^2/V s for MoS_2 and 7.32 cm^2/V s for ReS_2), large on/off ratio (~ 10^7). While Nourbakhsh et al. [174] was able to achieve a low off-current

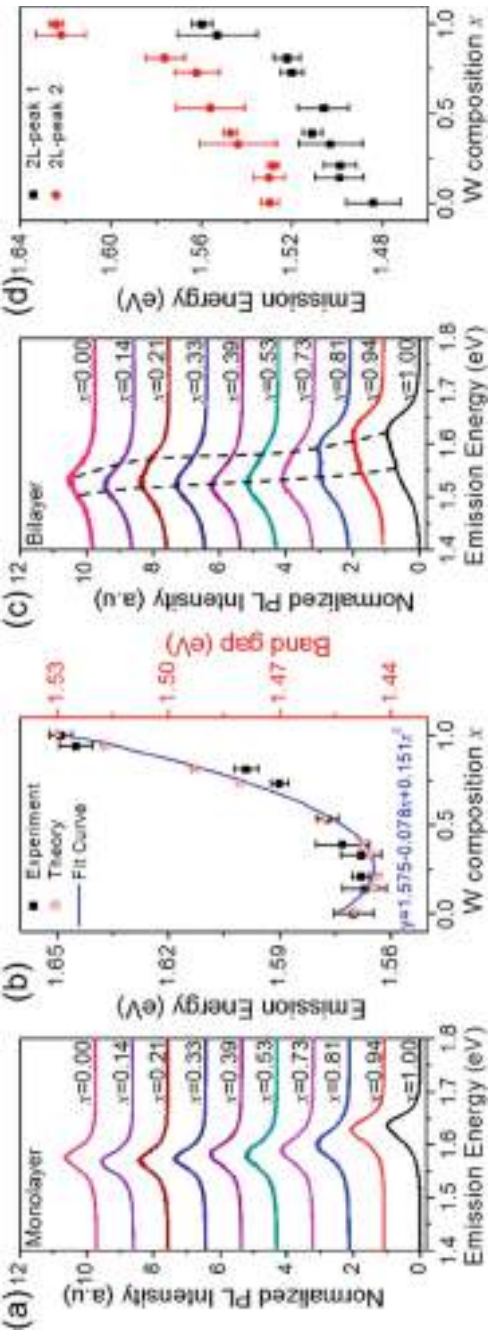

Fig. 31 **a** PL spectra and **b** PL emission energies of $Mo_xW_{1-x}Se_2$ monolayer alloys. The blue line in **b** is the parabola fitting for the experimental data. **c** PL spectra and **d** PL emission energies of $Mo_xW_{1-x}Se_2$ bilayer with composition. Reprinted from Zhang et al. [169], with permission from American Chemical Society. Copyright (2014)

of 10 pA/μm, an on/off current ratio of greater than 10^7, and a subthreshold swing of 120 μm dec^{-1} with 7.5 nm channel-length MoS_2 FET. This was indeed very difficult to realize due to the several challenges related to nanofabrication at this length scale. In case of another promising TMDC semiconductor WS_2, Aji et al. [175] realized high mobility (50 cm^2/V s) single-layer WS_2 using multilayer graphene as electrodes. In 2019, Gao et al. [176] proposed a MoS_2 based triboiontronic transistor for the first time using electric double layer FETs. Fabricating MoS_2/graphene heterostructure FETs based NO_2 gas sensors, it is possible to detect at low concentration upto 0.2 ppm [177]. Furthermore, Huang et al. [178] reported flexible sensitive pressure sensors based on MoS_2, WSe_2 transistors. Whereas Lee et al. [179] fabricated 2D vanadium carbide MXene (V_2 CT_X) based on sensitive gas sensor devices. These were capable to detect both polar and nonpolar chemical species including hydrogen and methane with a very low limit of detection of 2 and 25 ppm, respectively, at room temperature. Last but not least, we end this discussion by presenting an example of intriguing 2D tunneling transistors. Lin et al. [180] demonstrated quasi-heterojunction bipolar transistors using a monolayer of the lateral $WSe_2 - MoS_2$ junction. They explained the behavior of such transistors by resonant tunneling phenomenon.

5.4.2 Photovoltaic Cells, Light-Emitting Diodes, and Photodetectors

2D TMDC materials are considered as promising candidates for photovoltaic cells due to their large surface area, absence of dangling chemical bonds on surfaces with high potential as sunlight absorbers. In a conventional solar cell, a silicon homojunction is formed between two identical semiconductors having equal band gaps. The first graphene-Si heterojunction solar cell was reported on n-type Si by Li et al. [181]. The highly transparent graphene layer, as a conducting electrode, transmits a large amount of photons to the silicon active material. These photons after getting absorbed, excites a large number of electron–hole pairs. However, introducing a thin interlayer between the graphene and Si improves their overall performance [182]. Introducing a TMDC layer of MoS_2 also increases the efficiencies from 0.44 to 1.35% with monolayer, 5.98% with bilayer, and 8.0% for trilayer graphene [183].

A solar cell with a lateral monolayer MoS_2/WSe_2 interface was designed to achieve a power conversion efficiency of 2.56% under AM1.5G illumination [184]. In addition to this, the vertical heterostructure of MoS_2/WSe_2 is also used in the applications of lasers, light-emitting diodes (LED), and photovoltaic devices [185]. The MoS_2/Au based Schottky-barrier solar cell has demonstrated to have a PCE of 1.8%. The researches on TMDC-graphene vdW of varying thickness also have attracted insightful attentions. For example, WS_2/graphene based solar cell was able to yield a higher PCE of 3.3%. A high-performance Schottky-type solar cell has been constructed with few-layers of WSe_2 and WS_2 with the asymmetric contact of $Pd - WSe_2$ ($Ni - WS_2$) and $Ni - WSe_2$ ($Pt - WS_2$) [186].

Recently, graphene quantum dots have been introduced in the monolayer stack of a MoS_2/InP heterostructure solar cell, which showed an indication of improvement in the efficiency from 2.1 to 4.1% [187]. In addition, as shown in Fig. 33, monolayer

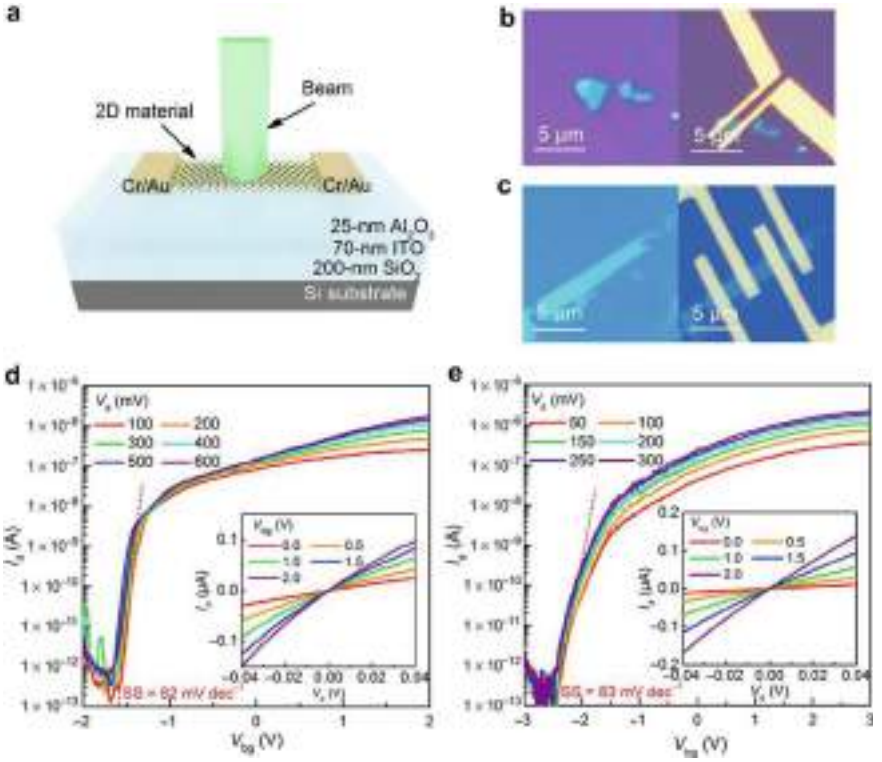

Fig. 32 **a** Schematic of a MoS_2 or ReS_2based FET on Al_2O_3/ITO/SiO_2/Si and the measurement setup. **b** Optical image of MoS_2 and the fabricated transistor. **c** Optical image of ReS_2 and the fabricated transistor. **d** MoS_2 FET: I_d–V_{bg} transfer curves in log scale. **e** ReS_2 FET: I_d–V_{bg} transfer curves in log scale. Reproduced from Xu et al. [173], under the Creative Commons Attribution Non Commercial License 4.0 (CC BY-NC). https://creativecommons.org/licenses/by-nc/4.0/

molybdenum disulfide MoS_2/InP heterostructures possess a remarkable photovoltaic response with PCE of 7.1% under AM1.5G illumination with a gate voltage of 6 V [188]. The tunable property of MoS_2/InP heterostructures may be promising for highly efficient solar cells. Furthermore, type II band alignment in Te/WTe_2 and Te/$MoTe_2$ heterojunction solar cells possess strong charge separation and enhanced sunlight absorption. The calculated maximum PCE of these kinds of materials are recorded to be as high as 22.5% and 20.1%, respectively. All these reported structures can be compatible with a variety of flexible and transparent substrates. If produced at low cost and large area, they will have various possible applications in the next generation flexible optoelectronic devices [189, 190].

We know that photodetection is the process in which a light signal is converted to an electrical signal. Since, the 2D semiconductors are atomically thin layers with favorable band gap values, they are considered promising materials for highly sensitive photodetection. In particular, monolayer transitional metal dichalcogenides

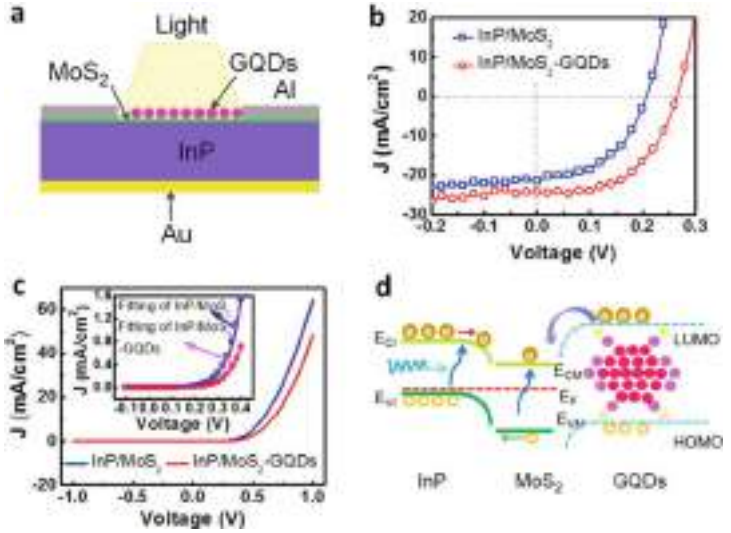

Fig. 33 **a** The schematic diagram representing MoS_2/InP solar cells with top graphene quantum dots (GQDs). Current density–voltage (J–V) curves of the monolayer MoS_2/InP solar cells under **b** AM1.5G illumination, **c** dark condition. **d** Band diagrams of monolayer MoS_2/InP interfaces with GQDs under illumination. Reprinted from Wang et al. [187], with permission from AIP Publishing. Copyright (2016)

exhibit strong light emission and absorption in the visible to near-infrared wavelength range, which make them attractive for optoelectronic applications [191]. Lai et al. [192] has fabricated metal-graphene oxide-metal photodetectors with specific detectivity of 3.31×10^7 Jones and responsivity of 23.6 mA W^{-1} under 1 V bias. Black phosphorene (BP) acts as a strong photo-device due to its high mobility of about 1000 cm^2 V^{-1} s^{-1}, and its direct band gap of (0.3–2) eV, depending on the number of layers [193]. Kwak et al. [194] has reported InP quantum dot/BP photodetector obtained responsivity of 109 A W^{-1}, ultrahigh detectivity of 4.5×10^{16} Jones with rise and fall times of 5 and 120 ms. Monolayer of MoS_2 photodetector has the shortest intrinsic response time of 3 ps [195, 196]. This implies a photodetection bandwidths as wide as 300 GHz for versatile applications. Particularly, the recently fabricated, layered $SnSe_2$ photodetector displays a good responsivity of 0.5 A/W and a fast photoresponse of about 2 ms at room temperature. This is one of the fastest response times among all types of 2D photodetectors. In addition, the ultrathin p-GaTe/n-MoS_2 vdW heterostructure has the rectification ratio, external quantum efficiency and photoresponsivity of 4:10:5, 61.68% and 21.83 A/W, respectively [197]. With all the progress in optoelectronic performances, these newly studied materials can effectively reduce the cost, improve large-scale production, and may be applied in wearable devices.

The light emission properties in 2D TMDCs are dominated by excitonic effects [198]. Electroluminescence is a physical phenomenon in which electrical energy

converts into optical energy resulting in the emission of light originating from the electron–hole recombination. In TMDCs, p- or n-types of doping can be easily realized, which benefit in constructing junctions for LEDs [199]. Two local gates forming a p–n junction can be used to build LEDs. As obtained, the LEDs based on bulk WSe_2 show outstanding performance with emission rate up to $\approx$ 16 million s^{-1} at applied current of 35 nA [200]. Polarized WSe_2-based LEDs were also reported, which can emit circularly polarized electroluminescence from p-i-n junction. Heterostructures based on TMDCs have also been developed for LEDs. A diode fabricated on a heavily p-type doped Si substrate, MoS_2/Si heterojunction, acts as an efficient LED [201] with a forward bias applied to the junction. The efficient radiative recombination originates from the direct band-gap of MoS_2 monolayer and the injection of holes from silicon across the junction. In addition, besides the conventional p–n junctions, vertical metal-insulator-semiconductor heterostructure can also be utilized to construct LEDs [202, 203]. In such a configuration of stacked graphene, h-BN and MoS_2 by Withers et al. construct a vertical heterostructure [204]. In this structure, two graphene layers act as the transparent electrodes, which were separated by an h-BN/MoS_2/h-BN sandwich arrangement. Electrons and holes tunnel through the h-BN layers to reach MoS_2 when an external bias is applied across the graphene layers. The external quantum efficiency of a single h-BN/MoS_2/h-BN was only $\approx$ 1% at low temperatures [204] which can be improved by stacking multiple layers together. This provides the injected carriers with additional chances to recombine radiatively with a rise in the efficiency of a device by $\approx$ 8.4%.

6 Future Prospective

It can be seen from our study that few organic, organic-inorganic hybrid peroskite and 2D semiconductors have emerged as future potential candidates for next-generation device applications. In case of organic semiconductors, we can mention the name of rubrene, CuPc, and pentacene whereas the notable candidates in 2D semiconductors are MoS_2, WS_2, and $MoSe_2$. In the case of hybrid perovskites, the mentionable candidates are $MASnI_3$, $FASnI_3$ and $(PEA)_2SnI_4$. Now, these materials with the value and nature of band gap, highest field-effect mobility (μ), and their applicability in various device purposes, are highlighted in Table 1.

We hope it will trigger the researchers to synthesize hybrid complex semiconductors with tunable band gaps suitable for device applications.

Table 1 A list of emergent semiconducting materials with the value and nature of band gap, highest field-effect mobility (μ), and their applicability in various device purposes

Material	Band gap (eV)	Direct/indirect nature	Highest μ (cm^2/V S)	Applicability
Rubrene	2.8 [203, 204]	Indirect [205]	20 [51]	OFET, OPV
CuPc	2.1 [206, 207]	Indirect [206, 207]	1 [208]	OFET, OPV, OLED
Pentacene	2.1–2.4 [209, 210]	Direct [209, 210]	2 [211]	OFET, OPV, OLED
$MASnI_3$	1.25 [108, 109, 212]	Direct [108, 109, 212]	2320 [213]	FET, PV, LED
$FASnI_3$	1.40 [108, 109, 212]	Direct [108, 109, 212]	103 [213]	FET, PV, LED
$(PEA)_2SnI_4$	1.97 [114]	Direct [114]	15 [214]	FET, PV, LED
MoS_2 (monolayer)	1.88 [215]	Direct [215]	1090 [216]	FET, PV, LED
WS_2 (monolayer)	2.03 [217]	Direct [217]	337 [218]	FET, PV, LED
Black phosphorene (monolayer)	1.88 [219]	Direct [219]	100 [220]	FET, PV

7 Concluding Remarks

In this chapter, we present the findings on the basis of our extensive literature survey on current advanced semiconductors. Several inorganic compounds and alloys, low-weight organic semiconductors, lower-toxic lead-free halide hybrid perovskites and beyond graphene 2D semiconducting materials, are included. Moreover, the chapter is dealing with a comprehensive study about the recent substantial researches on their electronic and the optical properties by complementary experimental and theoretical methods. These two properties are mostly crucial for understanding and optimizing functionality as well as performance of devices. Hence, discussions on the basis of the rigorous survey on recent vital progress of several electronic and optoelectronic devices (such as, LEDs, PV cells, photodetectors, FETs, sensors) have been presented. It is evident from our study that these modern semiconductors have sufficient potential to appear as prospective candidates in the field of flexible, light-weight, eco-friendly, and low-fabrication-cost future device applications. In brief, exploiting the properties of advanced semiconductors and translating them into device applications are common goals of the current semiconductor research community. We believe that the contents of the present chapter will be helpful to the readers to grasp the recent development in organic, inorganic and hybrid semiconductors.

Acknowledgements One of the authors (SS) gratefully acknowledges University Grants Commission [UGC] for providing financial assistance under D. S. Kothari Postdoctoral Fellowship Scheme [No. F.4-2/2006 (BSR)/PH/18-19/0073] whereas another author (SJ) acknowledges the Swami Vivekananda Merit Cum Means (SVMCM) scholarship scheme for providing research fellowship.

References

1. K.W. Böer, U.W. Pohl, *Semiconductor Physics*, 1st edn. (Springer, Cham, 2018), pp. 485–525
2. M. Grundmann, *The Physics of Semiconductors* (Springer, Cham, 2016), pp. 515–527
3. J.-H. Lee, J.-J. Kim, in *Physics of Organic Semiconductors*, 3rd edn., ed. by W. Brütting, C. Adachi (WILEY-VCH Verlag GmbH & Co. KGaA, Weinheim, 2012), pp. 91–118
4. A. Rodin, in *2D Semiconductor Materials and Devices*, ed. by D. Chi, K.E.J. Goh, A.T.S. Wee (Elsevier, 2019), pp. 1–23
5. M. Isshiki, J. Wang, in *Springer Handbook of Electronic and Photonic Materials*, ed. by S. Kasap, P. Capper (Springer, Cham, 2017), pp. 365–383
6. S. Adachi, in *Handbook of Electronic and Photonic Materials*, ed. by S. Kasap, P. Capper. *Springer Handbooks (SHB)* (Springer, Cham, 2017), pp. 726–741
7. C.Z. Ning, L. Dou, P. Yang, Nat. Rev. Mater. **2**, 17070 (2017)
8. S.M. Sze, *Physics of Semiconductor Devices* (Wiley, 1981), pp. 5–75
9. X. Zhang, D. Rao, R. Lu, K. Deng, D. Chen, AIP Adv. **5**, 057111 (2015)
10. A. De, C.E. Pryor, Phys. Rev. B **85**, 125201 (2012)
11. A. Srivani, V.R. Murthy, G.V. Raghavaiah, Int. J. Eng. Sci. **2**, 11 (2013)
12. R.H. Almadvari, M. Nayeri, S. Fotoohi, Mater. Res. Express **7**, 015915 (2020)
13. S.K. Tripathy, A. Pattanaik, Opt. Mater. **53**, 123 (2016)
14. S. Adachi, *Handbook on Physical Properties of Semiconductors* (Springer-Verlag, US, 2004), pp. 311–357
15. X. Liu, J.K. Furdyna, in *Chalcogenide*, ed. by X. Liu, S. Lee, J.K. Furdyna, T. Luo, Y.-H. Zhang. *Woodhead Publishing Series in Electronic and Optical Materials* (Woodhead Publishing, 2020), pp. 67–117
16. U. Chakma, A. Kumer, K.B. Chakma, T. Islam, D. Howlader, R. Mohamed, Eurasian Chem. Commun. **2**, 5 (2020)
17. N.H. Fares, N. Bouarissa, Mater. Res. **4**, 21 (2018)
18. G.D. Simoni, F. Paolucci, P. Solinas, E. Strambini, F. Giazotto, Nat. Nanotechnol. **13**, 802 (2018)
19. M.-F. Tsai, J. Jiang, P.-W. Shao, Y.-H. Lai, J.-W. Chen, S.-Z. Ho, Y.-C. Chen, D.-P. Tsai, Y.-H. Chu, ACS Appl. Mater. Interfaces **11**(29), 25882 (2019)
20. H. Oh, J. Park, W. Choi, H. Kim, Y. Tchoe, A. Agrawal, G.C. Yi, Small **14**, 1800240 (2018)
21. D. Fu, C. Zhu, X. Zhang, C. Li, Y. Chen, J. Mater. Chem. A **4**, 1390 (2016)
22. J. Ramanujam, U.P. Singh, Energy Environ. Sci. **10**, 1306 (2017)
23. M. Ravindirana, C. Praveenkumar, Renew. Sustain. Energy Rev. **94**, 317 (2018)
24. F.A. Jhuma, M.Z. Shaily, M.J. Rashid, Mater. Renew. Sustain. Energy **8**, 6 (2019)
25. S.-S. Sun, in *Introduction to Organic Electronic and Optoelectronic Materials and Devices*, 2nd edn., ed. by S.-S. Sun, L.R. Dalton (CRC Press, Boca Raton, 2016), pp. 53–53
26. H. Bronstein, C.B. Nielsen, B.C. Schroeder et al., Nat. Rev. Chem. **4**, 66–77 (2020)
27. D.-P. Han, G.W. Lee, S. Min, D.-S. Shin, J.-I. Shim, M. Iwaya, T. Takeuchi, S. Kamiyama, I. Akasaki, Sci. Rep. **10**, 17433 (2020)
28. Q. Zhang, W. Hu, H. Sirringhaus, K. Müllen, Adv. Mater. **34**, 2108701 (2022)
29. T.U. Kampen, *Low Molecular Weight Organic Semiconductors* (WILEY-VCH Verlag GmbH & Co. KGaA, Weinheim, 2010), pp. 85–118
30. I.E. Jacobs, A.J. Moulé, Adv. Mater. **29**, 1703063 (2017)

31. J.T.E. Quinn, J. Zhu, X. Li, J. Wang, Y. Li., J. Mater. Chem. C **5**, 8654 (2017)
32. S. Sinha, M. Mukherjee, J. Appl. Phys. **114**, 083709 (2013)
33. S. Sinha, C.H. Wang, M. Mukherjee, Thin Solid Films **638**, 167 (2017a)
34. S. Sinha, M. Mukherjee, Appl. Surf. Sci. **353**, 540 (2015a)
35. C. Emanuelsson, L.S.O. Johansson, H.M. Zhang, J. Chem. Phys. **149**, 164707 (2018)
36. D. Roy, S. Sinha, C.H. Wang, Y.W. Yang, M. Mukherjee, Langmuir **36**, 4607 (2020)
37. S. Sinha, A.K.M.M. Islam, M. Vorokhta, M. Mukherjee, J. Phys. Chem. C **121**, 3365 (2017b)
38. S. Feng, N. Luo, A. Tang, W. Chen, Y. Zhang, S. Huang, W. Dou, J. Phys. Chem. C **123**, 16614 (2019)
39. S. Haldar, S. Bhandary, H. Vovusha, B. Sanyal, Phys. Rev. B **98**, 085440 (2018)
40. K. Greulich, A. Belser, S. Bölke, P. Grüninger, R. Karstens, M.S. Sättele, R. Ovsyannikov, E. Giangrisostomi, T.V. Basova, D. Klyamer, T. Chassé, H. Peisert, J. Phys. Chem. C **124**(31), 16990 (2020)
41. M. Caputo, M. Panighel, S. Lisi, L. Khalil, G.D. Santo, E. Papalazarou, A. Hruban, M. Konczykowski, L. Krusin-Elbaum, Z.S. Aliev, M.B. Babanly, M.M. Otrokov, A. Politano, E.V. Chulkov, A. Arnau, V. Marinova, P.K. Das, J. Fujii, I. Vobornik, L. Perfetti, A. Mugarza, A. Goldoni, M. Marsi, Nano Lett. **16**(1), 3409 (2016)
42. M. Polek, F. Latteyer, T.V. Basova, F. Petraki, U. Aygül, J. Uihlein, P. Nagel, M. Merz, S. Schuppler, T. Chassé, H. Peisert, J. Phys. Chem. C **120**(43), 24715 (2016)
43. S. Mandal, M. Mukherjee, S. Hazra, ACS Appl. Mater. Interfaces **12**(40), 45564 (2020)
44. L. Zhang, T.L. Andrew, Org. Electron. **33**, 135 (2016)
45. M.R. Kiran, H. Ulla, Krishnamanohara, M.N. Satyanarayan, G. Umesh, Synth. Met. **269**, 116524 (2020)
46. P. Li, Z.-H. Lu, Adv. Mater. Interfaces **7**(17), 2000720 (2020)
47. C. Gaul, S. Hutsch, M. Schwarze, M. Schwarze, K.S. Schellhammer, F. Bussolotti, S. Kera, G. Cuniberti, K. Leo, F. Ortmann, Nat. Mater. **17**(5), 439 (2018)
48. S. Sinha, M. Mukherjee, Vacuum **148**, 48 (2018a)
49. S. Sinha, C.H. Wang, M. Mukherjee, Appl. Surf. Sci. **409**, 22 (2017c)
50. S. Sinha, M. Mukherjee, AIP Adv. **5**(10), 107204 (2015b)
51. V. Podzorov, E. Menard, A. Borissov, V. Kiryukhin, J.A. Rogers, M.E. Gershenson, Phys. Rev. Lett. **93**(8), 086602 (2004)
52. C.H. Wang, A.K.M.M. Islam, Y.W. Yang, T.Y. Wu, J.W. Lue, C.H. Hsu, S. Sinha, M. Mukherjee, Langmuir **29**(12), 3957 (2013)
53. S. Sinha, C.H. Wang, M. Mukherjee, T. Mukherjee, Synth. Met. **230**, 51 (2017d)
54. T. Mukherjee, S. Sinha, M. Mukherjee, Phys. Chem. Chem. Phys. **20**(27), 18623 (2018)
55. J.H. Oh, S. Liu, Z. Bao, R. Schmidt, F. Würthner, Appl. Phys. Lett. **91**, 212107 (2007)
56. M. Gsänger, J.H. Oh, M. Könemann, H.W. Höffken, A.-M. Krause, Z. Bao, F. Würthner, Angew. Chem. Int. Ed. **49**(4), 740 (2010)
57. B. Mukherjee, M. Mukherjee, ACS Omega **2**, 9181 (2017)
58. S. Sinha, C.H. Wang, M. Mukherjee, T. Mukherjee, Y.W. Yang, Langmuir **30**, 15433 (2014a)
59. S. Sinha, M. Mukherjee, Ind. J. Phys. **92**, 841 (2018b)
60. M. Zhang, Z. Hua, W. Liu, H. Liu, S. He, C. Zhu, Y. Zhu, J. Mol. Model. **26**, 32 (2020)
61. X. Wang, T. Garcia, S. Monaco, B. Schatschneider, N. Marom, CrystEngComm **18**, 7353 (2016a)
62. M.J. Waters, D. Hashemi, G. Shi, E. Kioupakis, J. Kieffer, J. Electron. Mater. **48**, 2962 (2019)
63. B.W. Caplins, T.K. Mullenbach, R.J. Holmes, D.A. Blank, Phys. Chem. Chem. Phys. **18**, 11454 (2016)
64. S. AlFaify, Y.S. Rammah, H.Y. Zahran, F. Yakuphanoglu, M. Shkir, Org. Opto-Elect. **2**, 1 (2016)
65. A. Baby, M. Gruenewald, C. Zwick, F. Otto, R. Forker, G. van Straaten, M. Franke, B. Stadtmüller, C. Kumpf, G.P. Brivio, G. Fratesi, T. Fritz, E. Zojer, ACS Nano **11**(10), 10495 (2017)
66. J. Li, G. D'Avino, A. Pershin, D. Jacquemin, I. Duchemin, D. Beljonne, X. Blase, Phys. Rev. Mater. **1**, 025602 (2017)

67. M.P. Ljungberg, O. Vänskä, P. Koval, S.W. Koch, M. Kira, D. Sánchez-Portal, New J. Phys. **19**, 033019 (2017)
68. M.R. Habib, H. Li, Y. Kong, T. Liang, Sk.Md. Obaidulla, S. Xie, S. Wang, X. Ma, H. Su, M. Xu, Nanoscale **10**(34), 16107 (2018)
69. E.P. Nguyen, B.J. Carey, C.J. Harrison, P. Atkin, K.J. Berean, E.D. Gaspera, J.Z. Ou, R.B. Kaner, K. Kalantar-zadeh, T. Daeneke, Nanoscale **8**(36), 16276 (2016)
70. H. Chang, W. Li, H. Tian, Y. Geng, H. Wang, D. Yan, T. Wang, Org. Electron. **20**, 43 (2015)
71. M.A. Fusella, S. Yang, K. Abbasi, H.H. Choi, Z. Yao, V. Podzorov, A. Avishai, B.P. Rand, Chem. Mater. **29**(16), 6666 (2017)
72. O.A. Melville, T.M. Grant, B. Mirka, N.T. Boileau, J. Park, B.H. Lessard, Adv. Electron. Mater. **5**, 1900087 (2019)
73. N.T. Boileau, R. Cranston, B. Mirka, O.A. Melville, B.H. Lessard, RSC Adv. **9**, 21478 (2019)
74. S. Sinha, C.H. Wang, M. Mukherjee, Y.W. Yang, J. Phys. D Appl. Phys. **47**, 245103 (2014b)
75. S. Sinha, C.H. Wang, M. Mukherjee, Physica E **93**, 39 (2017e)
76. O.A. Melville, B.H. Lessard, T.P. Bender, ACS Appl. Mater. Interfaces **7**, 13105 (2015)
77. Y. Sun, Q. Xie, Y. Zhu, L. Wang, Q. Sun, L. Wang, Appl. Surf. Sci. **505**, 144436 (2020)
78. M. Mirza, J. Wang, L. Wang, J. He, C. Jiang, Org. Electron. **324**, 96 (2015)
79. S. Wang, C. Chen, Z. Yu, Y. He, X. Chen, Q. Wan, Y. Shi, D.W. Zhang, H. Zhou, X. Wang, P. Zhou, Adv. Mater. **31**(3), e1806227 (2019a)
80. F. Dollinger, K.-G. Lim, Y. Li, E. Guo, P. Formánek, R. Hübner, A. Fischer, H. Kleemann, K. Leo, Adv. Mater. **31**(19), 1900917 (2019)
81. U. Zschieschang, H. Klauk, J. Mater. Chem. C **7**, 5522 (2019)
82. M.Y. Lee, H.R. Lee, C.H. Park, S.G. Han, J.H. Oh, Acc. Chem. Res. **51**, 2829 (2018)
83. W. Ke, D. Zhao, C.R. Grice, A.J. Cimaroli, G. Fang, Y. Yan, J. Mater. Chem. A **3**(47), 23888 (2015)
84. N. Torabi, A. Rahnamanic, H. Amrollahi, F. Mirjalili, M.A. Sadeghzade, A. Behjat, Org. Electron. **48**, 211 (2017)
85. B.-S. Kim, T.-M. Kim, M.-S. Choi, H.-S. Shim, J.-J. Kim, Org. Electron. **17**, 102 (2015)
86. X. Yang, G. Wang, D. Liu, Y. Yao, G. Zhou, P. Li, B. Wu, X. Rao, Q. Song, Curr. Appl. Phys. **18**, 1095 (2018a)
87. C. Wang, C. Li, G. Wang, C. Wang, P. Ma, L. Huang, S. Wen, W. Guo, L. Shen, S. Ruan, J. Phys. Chem. C **122**, 17110 (2018a)
88. R. Singh, J. Lee, M. Kim, P.E. Keivanidis, K. Cho, J. Mater. Chem. A **5**, 210 (2017a)
89. P. Qin, J. Zhang, G. Yang, X. Yu, G. Li, J. Mater. Chem. A **7**, 1824 (2018)
90. C.-J. Park, H.J. Park, J.Y. Lee, J. Kim, C.-H. Lee, J. Joo, ACS Appl. Mater. Interfaces **10**(35), 29848 (2018)
91. D. Jariwala, S. Howell, K.S. Chen, Nano Lett. **16**, 497 (2016)
92. Y. Yin, M.U. Ali, W. Xie, H. Yang, H. Meng, Mater. Chem. Front. **3**(6), 970 (2019)
93. Y. Liu, X. Wu, Z. Xiao, J. Gao, J. Zhang, H. Rui, X. Lin, N. Zhang, Y. Hua, S. Yin, Appl. Surf. Sci. **413**, 302 (2017a)
94. Q. Guo, H. Sun, J. Wang, D. Yang, J. Chen, D. Ma, J. Mater. Chem. C **4**, 376 (2016)
95. H. Sun, Q. Guo, D. Yang, Y. Chen, J. Chen, D. Ma, ACS Photon. **2**, 271 (2015)
96. D. Zhao, W. Huang, H. Guo, H. Wang, J. Yu, Mater. Sci. Eng. B **218**, 7 (2017a)
97. A. Salehi, X. Fu, D.-H. Shin, F. So, Adv. Funct. Mater. **29**, 1808803 (2019)
98. Y. Peng, R. Ding, Q. Ren, S. Xu, L. Sun, Y. Wang, F. Lu, Appl. Surf. Sci. **459**, 179 (2018)
99. C.W. Joo, J. Kim, J. Moon, K.M. Lee, J.-E. Pi, S.-Y. Kang, S.-D. Ahn, Y.-S. Park, D.S. Chung, Org. Electron. **70**, 101 (2019)
100. G. Simone, D.D.C. Rasi, X. de Vries, G.H.L. Heintges, S.C.J. Meskers, R.A.J. Janssen, G.H. Gelinck, Adv. Mater. **30**, 1804678 (2018)
101. J.S. Kim, Y.J. Choi, H.J. Woo, J. Yang, Y.J. Song, M.S. Kang, J.H. Cho, Adv. Funct. Mater. **27**(48), 1704475 (2017)
102. A. Pierre, I. Deckman, P.B. Lechêne, A.C. Arias, Adv. Mater. **27**(41), 6411 (2015)
103. T.M. Brenner, D.A. Egger, L. Kronik, G. Hodes, D. Cahen, Nat. Rev. Mater. **1**, 15007 (2016)

104. E.C. Schueller, G. Laurita, D.H. Fabini, C.C. Stoumpos, M.G. Kanatzidis, R. Seshadri, Inorg. Chem. **57**(2), 695 (2018)
105. Z. Shi, J. Guo, Y. Chen, Q. Li, Y. Pan, H. Zhang, Y. Xia, W. Huang, Adv. Mater. **29**(16), 1605005 (2017)
106. L. Ma, J. Dai, X.C. Zeng, Adv. Energy Mater. **7**, 1601731 (2017a)
107. J. Wang, J. Dong, F. Lu, C. Sun, Q. Zhang, N. Wang, J. Mater. Chem. A **7**, 23563 (2019b)
108. J. Wang, J. Dong, F. Lu, C. Sun, Q. Zhang, N. Wang, Adv. Mater. **32**, 2002717 (2020)
109. S. Tao, I. Schmidt, G. Brocks, J. Jiang, I. Tranca, K. Meerholz, S. Olthof, Nat. Commun. **10**, 2560 (2019)
110. V.N. Tuoc, T.D. Huan, J. Chem. Phys. **152**, 014104 (2020)
111. A. Stroppa, D. Di Sante, P. Barone, M. Bokdam, G. Kresse, C. Franchini, M.-H. Whangbo, S. Picozzi, Nat. Commun. **5**, 5900 (2014)
112. L. Ma, J. Dai, X.C. Zeng, Adv. Energy Mater. **7**, 1601731 (2017)
113. M. Roknuzzaman, C. Zhang, K. Ostrikov, A. Du, H. Wang, L. Wang, T. Tesfamichael, Sci. Rep. **9**, 718 (2019)
114. L. Lanzetta, J.M. Marin-Beloqui, I. Sanchez-Molina, D. Ding, S.A. Haque, ACS Energy Lett. **2**, 1662 (2017)
115. F. Yuan, X. Zheng, A. Johnston, Y.-K. Wang, C. Zhou, Y. Dong, B. Chen, H. Chen, J.Z. Fan, G. Sharma, P. Li, Y. Gao, O. Voznyy, H.-T. Kung, Z.-H. Lu, O.M. Bakr, E.H. Sargent, Sci. Adv. **6**, eabb0253 (2020)
116. H. Wang, Y. Chen, E. Lim, X. Wang, S. Yuan, X. Zhang, H. Lu, J. Wang, G. Wu, T. Lin, S. Sun, J. Wang, Y. Zhan, H. Shen, X. Menga, J. Chu, J. Mater. Chem. C **6**(46), 12714 (2018b)
117. Y. Gao, Z. Wei, P. Woo, E. Shi, M. Zeller, C. Zhu, P. Liao, L. Dou, J. Am. Chem. Soc. **141**(39), 15577 (2019a)
118. H.Y. Liang, F.L. Yuan, A. Johnston, C.C. Gao, H. Choubisa, Y. Gao, Y.-K. Wang, L.K. Sagar, B. Sun, P.C. Li, G. Bappi, B. Chen, J. Li, Y.K. Wang, Y.T. Dong, D.X. Ma, Y.N. Gao, Y.C. Liu, M.J. Yuan, M.I. Saidaminov, S. Hoogland, Z.-H. Lu, E.H. Sargent, Adv. Sci. **7**(8), 1903213 (2020)
119. W. Ke, C.C. Stoumpos, I. Spanopoulos, L. Mao, M. Chen, M.R. Wasielewski, M.G. Kanatzidis, J. Am. Chem. Soc. **139**(41), 14800 (2017a)
120. W. Ke, C.C. Stoumpos, M. Zhu, L. Mao, I. Spanopoulos, J. Liu, O.Y. Kontsevoi, M. Chen, D. Sarma, Y. Zhang, M.R. Wasielewski, M.G. Kanatzidis, Sci. Adv. **3**(8), e1701293 (2017b)
121. Z. Zhao, F. Gu, Y. Li, W. Sun, S. Ye, H. Rao, Z. Liu, Z. Bian, C. Huang, Adv. Sci. **4**(11), 1700204 (2017b)
122. M. Chen, Q. Dong, F.T. Eickemeyer, Y. Liu, Z. Dai, A.D. Carl, B. Bahrami, A.H. Chowdhury, R.L. Grimm, Y. Shi, Q. Qiao, S.M. Zakeeruddin, M. Grätzel, N.P. Padture, ACS Energy Lett. **5**(7), 2223 (2020)
123. K.S. Novoselov, A.K. Geim, S.V. Morozov, D. Jiang, Y. Zhang, S.V. Dubonos, I.V. Grigorieva, A.A. Firsov, Science **306**(5696), 666 (2004)
124. P. Nath, S. Chowdhury, D. Sanyal, D. Jana, Carbon **73**, 275 (2014)
125. S. Sinha, S. Pan, S. Choudhury, J. Sinha, A. Barman, J. Phys. Chem. C **121**, 17442 (2017f)
126. A. Bandyopadhyay, D. Jana, Rep. Prog. Phys. **83**, 056501 (2020)
127. S. Chowdhury, D. Jana, Rep. Prog. Phys. **79**, 126501 (2016)
128. A. Majumdar, S. Chowdhury, P. Nath, D. Jana, RSC Adv. **4**, 32221 (2014)
129. R. Das, N. Dhar, A. Bandyopadhyay, D. Jana, J. Phys. Chem. Solids **99**, 34 (2016)
130. Y. Zhang, A. Rubio, G.L. Lay, J. Phys. D Appl. Phys. **50**, 053004 (2017a)
131. B. Liu, A. Abbas, C. Zhou, Adv. Electron. Mater. **3**, 1700045 (2017b)
132. B.H. Nguyen, V.H. Nguyen, Adv. Nat. Sci. Nanosci. Nanotechnol. **7**, 043001 (2016)
133. A. Castellanos-Gomez, Nat. Photon. **10**, 202 (2016)
134. Q. He, Y. Liu, C. Tan, ACS Nano **13**, 12294 (2019)
135. Y. Zhang, A. Rubio, G.L. Lay, Phys. D Appl. Phys. **50**, 53004 (2017b)
136. D. Bhattacharya, D. Jana, Phys. Chem. Chem. Phys. **44**, 24758 (2019)
137. A. Bandyopadhyay, S. Datta, D. Jana, S. Nath, M.M. Uddin, Sci. Rep. **10**, 1 (2020)
138. S. Jana, A. Bandyopadhyay, D. Jana, Phys. Chem. Chem. Phys. **21**, 13795 (2019)